CLM-P825

# The LINDA Magnetic Geometry Interpolator

G. P. Maddison



UK ATOMIC ENERGY AUTHORITY

Culham Laboratory

CLM-P825

# The LINDA Magnetic Geometry Interpolator

G. P. Maddison

Culham Laboratory, Abingdon, Oxon OX14 3DB, UK
(UKAEA/Euratom Fusion Association)

ABSTRACT

More consistent numerical simulation of divertor tokamak edges relies on iteration of plasma and Monte Carlo neutral particle transport models in a common realistic geometry. Using existing HF magnetostatic equilibrium data, a new linear interpolation program denoted LINDA provides spatial discretisations everywhere closely aligned with axisymmetric magnetic structure. For a single-null poloidal divertor, chosen arrangements of piecewise linear magnetic flux surfaces are constructed, and deriving from a novel isosceles technique also orthogonal surfaces. Resulting grids are described explicitly in poloidal plane co-ordinates for neutral particle codes, and in fundamental metric functions detailing cell orthogonal diameters, interfacial areas and volumes for the BRAAMS steady-state plasma code. By imposing constant total and poloidal flux tube constraints and approximating connection length integrals, consistent specifications are determined simultaneously for both along magnetic field and poloidal cross-section co-ordinate versions. Example output for case NET-3A is presented. Expediting BRAAMS applications by evolving magnetic shear and extension to double-null configurations are considered.

Culham Laboratory
United Kingdom Atomic Energy Authority
Abingdon
Oxfordshire OX14 3DB

June, 1987

CONTENTS

## 1. INTRODUCTION

Where high temperature plasmas intercept material surfaces in the edge regions of magnetic confinement devices, a complex balance of anisotropic transport and interactions with recycled neutral particles determines the steady-state equilibria. Sophisticated computational models have been developed for each of these processes, typically describing plasma transport in terms of an Eulerian boundary value problem and using Monte Carlo sampling techniques to approximate atomic and molecular distributions.

Design studies of the poloidal divertor proposed for the NET tokamak principally are aimed at producing reliable predictions of its performance and characteristics, such as target power loadings, particle and energy exhaust, and so on. A particular goal is thus to improve the degree of consistency in its steady-state edge plasma simulations. Simply, the separate plasma transport and neutral particle codes should be iterated, each passing its output at each stage as input to the next generation of the other. Monte Carlo neutral particle simulators typically compute a linear approximation to the neutral distributions for a given invariant plasma background, and hence are already suited to such a cycle. The plasma transport component should be similarly adapted to attain solutions with corresponding fixed source terms. Assuming the latter to converge at each stage, new problems of stability and convergence of the overall procedure are clearly then defined. One consideration, for example, is the persistence of statistical errors in the neutral calculations. However, with some appropriate technique the fully consistent edge configuration, determined by the set of plasma, atomic and surface physics approximations and boundary conditions employed, can in principle be obtained for a specified divertor structure.

It is self-evident, but crucial, that this approach to consistency by definition relies on a common specification of system geometry between the component plasma and neutral calculations. Since each is certainly sensitive to geometric details, they must obviously both explore the same structure, and moreover, this structure must be as authentic as possible for the results to be genuinely representative. For neutral particles, with rectilinear trajectories between particle and surface collisions, a particular issue is accurate portrayal of the actual first wall and target shapes, but for the plasma, dominated by transport along magnetic field lines, the magnetic flux surfaces must be described. A necessary precursor to seeking consistent divertor calculations becomes the preparation of realistic geometric definitions in forms intelligible to both the plasma transport and neutral particle models.

For toroidally symmetric configurations such as poloidal divertors, a two-dimensional solution of the poloidal plane structure is required. The BRAAMS [1,2,3] (alternatively denoted BICEPS) two-dimensional transport code is expected to describe the dominant plasma effects appropriate to the collisional edge regions of large tokamaks like NET. Finite difference calculations are performed on a topologically rectangular mesh, which is related to an authentic poloidal geometry by specifying point by point transformation metric functions. In this report, we present an interpolation code, provisionally named LINDA, designed to produce the requisite functions from existing output of the HF[4] magnetostatic equilibrium code. Principal features of LINDA are piecewise linear approximations to poloidal magnetic flux surfaces, and using a novel geometric construction, orthogonal surfaces. Compatible representations of the geometry are determined simultaneously for both versions of BRAAMS

implemented alternatively in magnetic field line aligned and poloidal co-ordinates. Neutral particle simulators, for example DEGAS[5] or NIMBUS[6], typically express their discretised solution domain in explicit plane co-ordinates, and LINDA also generates a complete poloidal mesh declaration readily adaptable to any particular input form.

Introducing a fully authentic grid metric into BRAAMS implies a very significant increase in complexity of the solution region, and hence of the discretised correction equations prescribing relaxation to a steady-state plasma, over cases previously examined[3,7]. To minimise the complication, initial studies have consequently been based on the simpler single-null divertor concept. Grids are generated by a version of LINDA customised to the large aspect ratio, low beta NET-3A design. In fact, a double-null poloidal divertor is the preferred general arrangement for NET, and ultimately solutions for this problem are what is required. It is anticipated that preliminary single-null BRAAMS calculations will form a valuable and natural basis for subsequent double-null cases. Comparison of NET-3A BRAAMS simulations incorporating realistic geometry with previous results involving much simplified geometries should also highlight immediately just how sensitive are the steady-state plasmas to precise structural details. Furthermore, the essential interpolation approach adopted in LINDA should not be difficult to extend to other situations, including double-null divertors or limiters.

In detail, therefore, the new interpolation routine LINDA has been tailored specifically to provide the geometric information demanded by BRAAMS, and in Section 2 we first review its means of incorporating an arbitrary plane geometry. Attention is given to consistency between the alternative along field and poloidal cross-section co-ordinate representations. The piecewise linear interpolation of corresponding grids as implemented in LINDA is described in Section 3, focussing particularly on construction of co-ordinate lines everywhere orthogonal to magnetic flux surfaces. Examples of its output for a single-null divertor are also included. Finally, a short summary is presented, and some design study applications and extensions briefly anticipated, in Section 4.

## 2. REPRESENTATION OF PLANE GEOMETRIES IN BRAAMS

### 2.1 Control Volume Discretisation

Plasma transport is modelled in BRAAMS by equations expressing conservation of particles, momentum parallel to the magnetic field, and electron and ion energies, in conjunction with a diffusion relation for anomalous cross-field transport of ions[3]. A more detailed exposition of these equations is not actually necessary, it being sufficient for present purposes merely to consider the means by which they are recast into a form amenable to numerical solution.

Following Patankar[8], it is useful first to recall the discrete conservation relation governing an arbitrary extensive quantity $\phi$ subject to generalised convection and conduction through an elementary physical volume V in some orthogonal right-handed curvilinear co-ordinate frame $(\sigma_x, \sigma_y, \sigma_z)$. Here the restriction to orthogonal co-ordinates is crucial, in order that motion in one co-ordinate direction is always normal to the other two. This condition ensures that in a lattice of volume elements all fluxes are wholly specified between each cell and those neighbouring its faces, rather

than involving others adjoining just its edges as well. Never-the-less, there are some unfortunate consequences for simulation of plausible divertor arrangements, as discussed further in Section 3 later. Now let faces respectively normal to the $\sigma_x$-, $\sigma_y$-, $\sigma_z$-axes have elementary areas $a_x$, $a_y$, $a_z$, and denote the convective velocity vector $(\upsilon_x, \upsilon_y, \upsilon_z)$. Over a short time interval $\tau$ the increment in $(\rho\phi)$, where $\rho$ is mass density, is of course given by the discrete divergence of the total combined flux through V, plus any included source or sink contributions. Explicity, restricting to planar variations having absolutely no gradients with respect to $\sigma_z$, one has:-

$$d(\rho\phi) = \frac{\tau}{V} \{ (\upsilon_x \rho\phi a_x)_{\sigma_x} - (\upsilon_x \rho\phi a_x)_{\sigma_x + d\sigma_x} + (\upsilon_y \rho\phi a_y)_{\sigma_y} - (\upsilon_y \rho\phi a_y)_{\sigma_y + d\sigma_y}$$

$$- (a_x \Lambda_x \nabla_{\sigma_x} \phi)_{\sigma_x} + (a_x \Lambda_x \nabla_{\sigma_x} \phi)_{\sigma_x + d\sigma_x} - (a_y \Lambda_y \nabla_{\sigma_y} \phi)_{\sigma_y} + (a_y \Lambda_y \nabla_{\sigma_y} \phi)_{\sigma_y + d\sigma_y} + VS \}, \quad (1)$$

where $\Lambda_x$; $\Lambda_y$ are generalised conduction coefficients, here with dimensions of dynamic viscosity, and the source term S is expressed per unit volume per unit time.

For a full poloidal divertor tokamak, ignoring magnetic field ripple and diamagnetic flows, it is evident in view of its toroidal symmetry that its edge plasma transport is an anisotropic two-dimensional phenomenon, as supposed in (1) above. Quantities propagate rapidly along magnetic field lines and much more slowly in an essentially minor radial normal direction, with uniformity being presumable in the third redundant dimension. Moreover, each Boltzmann moment equation for particle number density, momentum and energy, conventionally closed, obtains basically a convection and conduction form[9], further as exemplified in (1). Such a model, as is indeed embodied in the BRAAMS code[3], thus requires geometric information designating a particular solution space as manifested in (1).

In BRAAMS, the solution domain is divided into a topologically rectangular mesh[3], each cell of which corresponds to an individual volume element as considered for (1). It is apparent that an extent in the ignorable ($\sigma_z$) co-ordinate dimension is implied. Means of interpreting and assigning this dimension are postponed to sub-section 2.2, while presently we merely assert that it should be finite but not constant. Finite difference forms of each plasma transport equation over the grid are then deduced precisely in the manner of (1), namely effecting respective conservation principles over its discrete units. A possible viewpoint is that this construction obviously is equivalent to integrating the differential moment equations over each separate cell[3,8], although as remarked by Patankar[8] this is really somewhat perverse, since it is the differential relations themselves which strictly derive from an analytic limit of finite expressions like (1). To convey its essential feature, the resulting representation is denoted the "control volume" formulation or discretisation[8].

Hence the finite difference equations to be solved numerically in BRAAMS are mapped to a given physical structure by supplying those functions occurring in the general form (1) which define its geometry. Cell to cell interfacial areas ($a_x$; $a_y$) and volumes (V) are required, and in addition a means of specifying gradients ($\nabla_{\sigma_x}$; $\nabla_{\sigma_y}$). A minor complication here is that as demonstrated in (1), these must be evaluated where fluxes enter and leave a cell, namely at cell <u>faces</u>. However, it may be envisaged that if face to

face physical diameters in the $\sigma_x$- and $\sigma_y$- directions across each cell are known, some appropriate interpolation should furnish an estimated inverse physical length, and so a discrete gradient denominator, at interfacial positions. In other words, the pair of cell widths completes the necessary set of geometric data.

A more formal elucidation may be obtained by recalling a regular Cartesian reference frame (x,y,z) may be transformed into a right-handed curvilinear co-ordinate frame $(\sigma_x,\sigma_y,\sigma_z)$ according to a metric tensor $g_{ik}(\sigma_x,\sigma_y,\sigma_z)$, where i,k = 1,2,3 signify respectively $\sigma_x$, $\sigma_y$, $\sigma_z$ components. Two points displaced by small increments in each co-ordinate are then separated by a distance element ds, given by[10]:-

$$ds^2 = dx^2 + dy^2 + dz^2 = \sum_{i=1}^{3} \sum_{k=1}^{3} g_{ik}(\sigma_x,\sigma_y,\sigma_z)\, d\sigma_i d\sigma_k . \qquad (2)$$

If in addition $\sigma_x,\sigma_y,\sigma_z$ are orthogonal, then $g_{ik}$ is diagonal and may be written:-

$$\underline{\underline{g}} = \begin{pmatrix} h_x^2 & 0 & 0 \\ 0 & h_y^2 & 0 \\ 0 & 0 & g/h_x^2 h_y^2 \end{pmatrix}, \qquad (3)$$

where $1/\sqrt{g}$ is the Jacobian of the transformation. From (2) and (3), small projections separately in each curvilinear direction now correspond to physical dimensions:-

$$ds_x = h_x d\sigma_x \quad ; \quad ds_y = h_y d\sigma_y \quad ; \quad ds_z = \frac{\sqrt{g}}{h_x h_y}\, d\sigma_z . \qquad (4)$$

Recalling associated magnitude of surface area and volume elements are determined[10]:-

$$dA_j = \sqrt{g_{ii} g_{kk}}\, d\sigma_i d\sigma_k = ds_i ds_k \quad ; \quad dV_o = \frac{\partial(x,y,z)}{\partial(\sigma_x,\sigma_y,\sigma_z)}\, d\sigma_x\, d\sigma_y\, d\sigma_z , \qquad (5)$$

they become also:-

$$dA_x \equiv a_x = \frac{\sqrt{g}}{h_x}\, d\sigma_y d\sigma_z = ds_y ds_z \quad ; \quad dA_y \equiv a_y = \frac{\sqrt{g}}{h_y}\, d\sigma_x d\sigma_z = ds_x ds_z \quad ;$$

$$dA_z \equiv a_z = h_x h_y d\sigma_x d\sigma_y = ds_x ds_y \quad ; \qquad (6)$$

$$dV_o \equiv V = \sqrt{g}\, d\sigma_x d\sigma_y d\sigma_z = ds_x ds_y ds_z .$$

Expressions (4) and (6) may be inserted into discrete approximations for three-dimensional changes to general variables in the $(\sigma_x,\sigma_y,\sigma_z)$ co-ordinate frame, to recover in the analytic limit familiar curvilinear differential forms. Firstly, for a scalar quantity $\phi$ they yield components:-

$$\nabla\phi \approx \left(\frac{1}{ds_x} d\phi \Big|_{\sigma_y,\sigma_z}, \frac{1}{ds_y} d\phi \Big|_{\sigma_x,\sigma_z}, \frac{1}{ds_z} d\phi \Big|_{\sigma_x,\sigma_y}\right)$$
$$\rightarrow \left(\frac{1}{h_x}\frac{\partial\phi}{\partial\sigma_x}, \frac{1}{h_y}\frac{\partial\phi}{\partial\sigma_y}, \frac{h_x h_y}{\sqrt{g}}\frac{\partial\phi}{\partial\sigma_z}\right). \quad (7)$$

A related treatment for a vector quantity may be inferred by considering exclusively the divergence part for $(\rho\phi\underline{v}) \equiv \underline{F} = (F_x, F_y, F_z)$ in a full three-dimensional analogue of (1), ignoring also time integration, i.e:-

$$\nabla.\underline{F} \approx \frac{1}{\sqrt{g}\, d\sigma_x d\sigma_y d\sigma_z} \left\{ d\left(F_x \frac{\sqrt{g}}{h_x}\right) d\sigma_y d\sigma_z \Big|_{\sigma_y,\sigma_z} + d\left(F_y \frac{\sqrt{g}}{h_y}\right) d\sigma_x d\sigma_z \Big|_{\sigma_x,\sigma_z} + d\left(F_z h_x h_y\right) d\sigma_x d\sigma_y \Big|_{\sigma_x,\sigma_y} \right\} \quad (8)$$

$$\rightarrow \frac{1}{\sqrt{g}} \left\{ \frac{\partial}{\partial\sigma_x}\left(F_x \frac{\sqrt{g}}{h_x}\right) + \frac{\partial}{\partial\sigma_y}\left(F_y \frac{\sqrt{g}}{h_y}\right) + \frac{\partial}{\partial\sigma_z}\left(F_z h_x h_y\right) \right\}.$$

Working backwards from (7) and (8), and recollecting the general two-dimensional convection and conduction type as in (1) which characterises each plasma transport equation comprising the BRAAMS model, it is quite apparent that the set of geometric details required to map its discrete computational mesh into a selected physical region is just as previously stated. To summarise, therefore, cell by cell widths ($ds_x$; $ds_y$), and interfacial areas ($a_x$; $a_y$) and volumes (V) consistent according to (6), must be tabulated. Formally, this procedure may be regarded as defining the fundamental metric functions $h_x; h_y; \sqrt{g}$ over the grid.

## 2.2 Along field and poloidal co-ordinates

Owing to their toroidal symmetry, the poloidal divertor systems of interest are expected to be intrinsically two-dimensional in their behaviour. A control volume formulation of the pertinent plasma transport equations solved numerically in BRAAMS clearly relies then on specifying a cell extent, $\Delta s_z$ say, in the ignorable co-ordinate ($\sigma_z$) direction. How $\Delta s_z$ varies over the calculation mesh depends on how the solution co-ordinate frame $(\sigma_x, \sigma_y, \sigma_z)$ is oriented with respect to toroidal symmetry.

Primarily, plasma flows proceed along magnetic field lines, with relatively much constrained perpendicular progress minor radially across them. The co-ordinate alignment thus most naturally suggesting itself is one having $\sigma_x$- and $\sigma_y$- dimensions as far as possible respectively parallel to these directions. Remembering strict requirement of an orthogonal system, in this case $ds_x$ for each cell corresponds to its actual face to face magnetic connection length, while $ds_y$ indicates its width in a surface everywhere orthogonal to magnetic flux surfaces and predominantly aligned with local cross-field transport except possibly around magnetic field

singularities (X-points). The totally symmetric $\sigma_z$- direction is always normal to such a field line containing $(\sigma_x, \sigma_y)$ surface, and so varies in a complicated fashion with q-factor along any given solution plane locus. One interesting corollary is that Lorentz magnetic forces on each plasma species always lie along $\sigma_z$ and, independent of any other assumptions, are automatically excluded from the picture.

A first version of BRAAMS has been implemented precisely in magnetic field line directed co-ordinates[1,2]. For this along field realisation, $\Delta s_z$ actually assumes a rather simple interpretation. Since any grid row, equivalent to a $\sigma_y$ = constant curve, traces total magnetic induction from point to point, its normal cross-section $a_x$ clearly represents a discrete flux tube. If $ds_y$ is determined by flux surface interspacings, $\Delta s_z$ is consequently fixed at each point by a condition of constant intercepted total flux (cf(6)), viz:-

$$Ba_x = \text{constant} \Rightarrow \quad \Delta s_z(\sigma_x, \sigma_y) = \frac{B(0, \sigma_y)}{B(\sigma_x, \sigma_y)} \frac{ds_y(0, \sigma_y)}{ds_y(\sigma_x, \sigma_y)} \Delta s_z(0, \sigma_y). \qquad (9)$$

Only an overall row normalisation $\Delta s_z(0, \sigma_y)$ remains to be set; unity is perhaps a suitable value. Equation (9) with (6) suffices to enable complete specification of an along field grid metric germane to realistic BRAAMS simulations.

Although along field co-ordinates plainly seem an efficient approach to describing plasma behaviour, they are manifestly unsatisfactory in one crucial respect. Neutral particles recyling from impacted material surfaces, principally the divertor targets, and providing sources or sinks of ions, momentum and energy where they interact with plasma particles, are of course oblivious to magnetic fields. Following rectilinear trajectories between interactions, they permeate potentially the entire torus and divertor interiors. Now their toroidally symmetric distributions reflect expressly the enclosing first wall poloidal structure, and are efficiently representable only in a poloidal plane projection itself. In other words, their inherent ignorable co-ordinate is explicity toroidal. Most importantly, a two-dimensional Monte Carlo calculation of recycling neutral particle distributions would have to explore exactly the symmetric poloidal cross-section of any given divertor arrangement. While some adjustment may be envisaged of a simplified neutral source model invoked in BRAAMS to fit it into an along field calculation, therefore, for eventual iteration with accurate neutral simulations as intended poloidal co-ordinates are imperative.

To discern steady-state plasmas in poloidal co-ordinates, a possible method would be to project converged BRAAMS solutions in the along field frame into a poloidal cross-section. Both internal neutral treatments and subsequent iterations with Monte Carlo computed neutral distributions still would involve projecting these in turn back into along field co-ordinates again. Clearly, a more efficient procedure ultimately is to execute BRAAMS in the poloidal plane also. It is important to appreciate that no modification is implied in the actual plasma transport model, since physically a situation of fluxes predominantly parallel to magnetic field lines of course still prevails. In particular, momentum balance within magnetic flux surfaces still applies in terms of an along field quantity.

Each moment equation is merely recast by a co-ordinate deformation, equivalent to a rotation at each point about a $\sigma_y$-axis, bringing $\sigma_x$ everywhere from along the magnetic field into the poloidal plane[3]. Simultaneously $\sigma_z$ becomes everywhere toroidally directed. Control volume finite difference expressions as in (1) are again constructed for the newly oriented cells, and solved numerically in BRAAMS as before. Above all, this technique hence continues to exclude diamagnetic flows, even though physically these do now have non-vanishing components within the solution plane. Such an approximation remains potentially crude only where convective velocities otherwise become very small in magnitude, and in any case may be removed in some future extension of BRAAMS.

A poloidal version of BRAAMS as outlined above has also been implemented[3]. Let terms pertaining to along field and poloidal reference frames hereafter be denoted by superscripts F and P respectively. As implied, $\sigma_y^P \equiv \sigma_y^F$ retains its original identity, being always normal to magnetic flux surfaces. Consistent discretisations of a given toroidally symmetric structure into along field and poloidal BRAAMS grids thus have equal cross-field widths $ds_y^P \equiv ds_y^F$. On the other hand, $\sigma_x^P$ now lies along magnetic flux surfaces in the poloidal plane, so that infinitesimal extents $\delta s_x^P$; $\delta s_x^F$ must be related by a projection:-

$$\delta s_x^P = \frac{B_\theta}{B}\,\delta s_x^F = \frac{B_\theta}{B}\,h_x^F \delta\sigma_x^F, \qquad (10)$$

where $B_\theta$;B are respectively local magnitudes of poloidal and total magnetic induction, and we have recalled (4). Allowing for variations spanned in magnetic field line pitch angle $\alpha = \cos^{-1}(B_\theta/B)$, consistent discrete grid cell widths are given by:-

$$ds_x^P = ds_x^F \left(\frac{1}{ds_x^F}\int_0^{ds_x^F} \frac{B_\theta}{B}\,ds_x^F\right) = \int_{\sigma_x^F}^{\sigma_x^F + d\sigma_x^F} \frac{B_\theta}{B}\,h_x^F d\sigma_x^F. \qquad (11)$$

This generalisation is especially important for divertor configurations, as changes in poloidal field strength ($B_\theta$) gradient near their X-points can be substantial. To complete the metric one must set finally $\Delta s_z^P$, which at first may seem less obviously determined.

The crucial point is to produce along field and poloidal mesh geometries consistent in the sense that BRAAMS calculations in both co-ordinate systems with identical boundary conditions would result in identical steady-state plasmas. Logically, such agreement would seem to follow if cell to cell interfacial areas are chosen so as to preserve absolute fluxes through them in each case. In other words, observing from (10) that $v_x^P = (B_\theta/B)\,v_x^F$ and using (6), once more considering an arbitrary extensive quantity $\phi$ we impose (see FIG.1):-

$$v_x^P\,\rho\phi\,ds_y^P\Delta s_z^P = v_x^F\,\rho\phi\,ds_y^F\Delta s_z^F \Rightarrow\quad a_x^P = \frac{B}{B_\theta}\,a_x^F\ ;\ \Delta s_z^P = \frac{B}{B_\theta}\,\Delta s_z^F. \qquad (12)$$

Note unlike in (11), here variation of $\alpha$ with $\sigma_y$ is neglected, since $ds_y < ds_x$ usually. Equation (12) describes the toroidal extent of a poloidal cell at its magnetic flux surface normal faces $(\sigma_x^P;\ \sigma_x^P + d\sigma_x^P)$. A similar condition on cross-field fluxes strictly yields an extent also associated with its ostensibly parallel faces $(\sigma_y^P;\ \sigma_y^P + d\sigma_y^P)$:-

$$v_y^P\ \rho\phi ds_x^P \Delta s_z^P = v_y^F\ \rho\phi ds_x^F \Delta s_z^F \Rightarrow\ a_y^P = a_y^F\ ;\ \Delta s_z^P = \left(\frac{\overline{B_\theta}}{B}\right)^{-1} \Delta s_z^F, \qquad (13)$$

whence a mean magnetic pitch as defined in (11) is accordingly recovered over the cell longitudinal dimension. From (12) one finds that by so choosing $\Delta s_z^P$, equal magnetic flux products are intercepted by corresponding grid rows in the two frames $a_x^P B_\theta = a_x^F B$. Now by a flux tube construction (9), the latter along field product is a constant, and hence each grid row in poloidal co-ordinates is an equivalent tube of constant poloidal, i.e. projected, flux. Analagously to (9) we may write:-

$$\Delta s_z^P(\sigma_x^P, \sigma_y^P) = \frac{B_\theta(0, \sigma_y^P)}{B_\theta(\sigma_x^P, \sigma_y^P)}\ \frac{ds_y^P(0, \sigma_y^P)}{ds_y^P(\sigma_x^P, \sigma_y^P)}\ \Delta s_z^P(0, \sigma_y^P)\ , \qquad (14)$$

where again an overall normalisation $\Delta s_z^P(0, \sigma_y^P)$ should strictly be ascribed in compliance with (12).

A further connotation of (13) and (6) connects cell volumes in either co-ordinate system, viz:-

$$V^P = \sqrt{g^P}\ d\sigma_x^P d\sigma_y^P d\sigma_z^P = ds_x^P ds_y^P \Delta s_z^P = \left(\frac{\overline{B_\theta}}{B}\right) ds_x^F ds_y^F \left(\frac{\overline{B_\theta}}{B}\right)^{-1} \Delta s_z^F =$$
$$\sqrt{g^F}\ d\sigma_x^F d\sigma_y^F d\sigma_z^F = V^F. \qquad (15)$$

Each cell volume is preserved, therefore, through rotation from along field to poloidal orientation. In an analytic limit of infinitesimal neighbourhoods of any given point, the Jacobians for each transformation to along field and poloidal frames are equal $1/\sqrt{g^P} = 1/\sqrt{g^F}$, as is indeed required for frames related locally simply by a rotation about a common axis. This constraint could conversely have been employed to derive (13). Similarly, yet another viewpoint is exposed by referring to the usual magnetostatic equilibrium formula for $B_\theta$ with toroidal symmetry [11]. If $R;\zeta$ denote respectively major radial and orthogonal azimuthal co-ordinates and $\psi(R,\zeta)$ the poloidal flux function then:-

$$B_\theta = \frac{1}{R} \sqrt{\overline{\left(\frac{\partial\psi}{\partial R}\right)^2 + \left(\frac{\partial\psi}{\partial\zeta}\right)^2}} = \frac{1}{R} \sqrt{\overline{\nabla\psi . \nabla\psi}}. \qquad (16)$$

But in our poloidal cross-section co-ordinates $\sigma_x^P$ by construction lies always within magnetic flux surfaces and $\sigma_y^P$ orthogonal to them, so that poloidal flux surfaces are actually curves of constant $\sigma_y^P$, or $\psi = \psi(\sigma_y^P)$. Thus expressing $\nabla\psi$ in this frame produces:-

$$B_\theta = \frac{1}{R} \left| \frac{1}{h_y^P} \frac{\partial\psi}{\partial\sigma_y^P} \right| . \qquad (17)$$

For any grid row, representing a course between two magnetic flux surfaces, $\psi$ everywhere exhibits a fixed increment $d\psi$ across it, and discretising (17) in a constant poloidal flux tube proposition as (12) leads to:-

$$B_\theta a_x^P = \frac{1}{R} \frac{1}{ds_y^P} d\psi \; ds_y^P \Delta s_z^P = \text{constant} \Rightarrow \Delta s_z^P(\sigma_x^P, \sigma_y^P) = \frac{R(\sigma_x^P, \sigma_y^P)}{R(0, \sigma_y^P)} \Delta s_z^P(0, \sigma_y^P) . \qquad (18)$$

Our previous assertion to maintain plasma fluxes (12) is consequently equivalent to each cell in a given poloidal grid row having a toroidal extent proportional to that whole toroidal element length $2\pi R$ generated by revolution about the centre line. In an axisymmetric situation this manifestly seems reasonable. An incidental result inferred in passing from (16) and (17) is the metric relationship:-

$$\frac{1}{h_y^P} \equiv \sqrt{\left(\frac{\partial\sigma_y^P}{\partial R}\right)^2 + \left(\frac{\partial\sigma_y^P}{\partial\zeta}\right)^2} . \qquad (19)$$

To summarise, basic grid metric functions differ between along field and poloidal representations only in longitudinal cell extents $ds_x$ (cf(11)) and interfacial areas $a_x$ (cf (12)); magnetic flux surface orthogonal extents $ds_y$, interfacial areas $a_y$ and cell volumes V are equal in both cases. One additional requirement for BRAAMS calculations in poloidal co-ordinates is a description of $(B_\theta/B)$ over the mesh, in order explicitly to project magnetic field line directed velocity, pressures and transport coefficients at each point into the solution plane[3]. As with discrete gradient denominators, it is sufficient to recount this pitch angle variable just at cell centres and later interpolate values when needed at intervening positions.

## 3. DISCRETISATION OF MAGNETIC GEOMETRIES

### 3.1 The LINDA Interpolation Code

In order to prescribe a desired geometry in a BRAAMS plasma transport calculation, as seen above cell by cell metric functions mapping its rectangular calculational mesh into the physical region must be specified. For an associated Monte Carlo neutral particle calculation, an exactly corresponding geometry is generally derivable from a description simply in plane co-ordinates of each cell vertex in this discretised solution space[5,6]. Improving consistency in both instances by refining the geometry involved should first of all discover any deficiencies in existing cases based on simplified representations[7]. Moreover, for their eventual iteration necessarily with a single common geometry, its refinement is essential to justify and to validate such a demanding approach to self-consistency. For both these reasons, it is most important to provide for physical discretisations which are as authentic as possible.

Now there is readily available existing output from the HF magnetostatic equilibrium code[4] for many proposed NET poloidal divertor configurations. Assuming perfect axisymmetry, a regular rectangular lattice in major radial and azimuthal co-ordinates $(R,\zeta)$ is superimposed on a poloidal cross-section. Data matrices of poloidal magnetic flux function $\psi(R,\zeta)$ in Volt.seconds and cotangent of field line pitch angle $\cot\alpha = (B_\theta/B_\phi)$, where $B_\theta$; $B_\phi$ are respectively magnitudes of local poloidal and toroidal magnetic induction, are generated over the lattice. Hence, arbitrary orthogonal grids aligned with actual magnetic flux surfaces in a given divertor arrangement, as previously shown to be required, may be deduced by interpolating these data. Their accompanying metric functions are immediately appropriate to the poloidal co-ordinates version of BRAAMS, and using (11) and (12) may simultaneously be consistently expressed for the along field co-ordinates version. Recording $(R,\zeta)$ co-ordinates of every cell vertex should also be sufficient to supply the grids later to neutral particle simulations.

The philosophy adopted was to interpolate the required metric designations closely approximating actual magnetic geometries in selected poloidal divertor arrangements, while accepting established HF solutions as a "black box". In other words, an option to modify HF to produce alternative output and then to repeat calculations was deliberately avoided. This simplified the overall undertaking in that only two major codes, for plasma and neutral particle transport, are involved, and does not anyway necessarily imply any greater crudity in interpolating magnetic structures. An argument that other information regarding $\nabla\psi$ at each lattice point would improve estimation of magnetic flux orthogonal surfaces, for instance, is contested in sub-section 3.3 below. A principle of consistency of approximation through-out was also assumed. Thus, piecewise linear interpolation of all quantities at all points is suggested, because of its simplicity, robustness, proof against spurious turning points between end values, and because here no other higher order form is actually any better justified in general. The new procedure resulting interfaces between HF and BRAAMS or a Monte Carlo neutral particle code, and to convey foregoing attributes embodied has provisionally been named LINDA (Linearly Interpolated Numerical Divertor Architecture).

In NET, the preferred magnetic divertor structure is in fact a double-null form, owing to its potential advantages for example with respect to target loading. Never-the-less, it was decided initially to address an intrinsically simpler single-null divertor problem, so as to introduce greater complexity compared with previous BRAAMS cases[7] in a more gradual manner. At each iteration within a BRAAMS calculation, from the set of moment transport equations comprising its model are derived discretised correction equations, solution of which is designed to reduce current estimates of conservation violating residuals[1,2,3]. A refined geometry, through its metric functions, complicates the block-banded matrix forms of these discrete equations, inhibiting both their solution at each stage and overall convergence to an internally consistent plasma steady state. Clearly it is sensible, therefore, to exacerbate these difficulties by degrees, while simultaneously expecting a single-null divertor should be a most natural step to the double-null goal. Similarly, a single-null configuration with no extreme magnetic flux surface curvatures or highly compressed regions would be preferrable, to facilitate interpolation. For

such reasons, then, first studies have been based on NET-3A, a low triangularity, high aspect ratio, low beta single-null design, and for which, moreover, BRAAMS results with approximate geometries are already available[7]. In the following description of how interpolation of magnetic geometries has been implemented, reference is made primarily to a version of LINDA specially customised to this NET-3A divertor, but underlying generality of methods where appropriate should be borne in mind. Most importantly, of course, attention is particularly drawn to key areas affecting extension to double-null divertors.

### 3.2 Poloidal Magnetic Flux Surfaces

Executing BRAAMS in an along field frame, the longitudinal co-ordinate $\sigma_x^F$ is everywhere parallel to a total magnetic induction direction vector $(\underline{B}/B)$, while in a poloidal frame its counterpart $\sigma_x^P$ follows contours of constant poloidal flux $\psi$. In either case, $\sigma_x$ lies always within the axisymmetric poloidal magnetic flux surfaces. Thus to infer realistic computational geometries, firstly one must delineate these prevailing superficies.

Numerically, one wants to identify an ordered set of poloidal plane co-ordinates $\{(R_i,\zeta_i)\}_i$ which when connected in sequence by straight-line segments produce a piecewise linear approximation to a given flux surface. Any chosen solution space discretisation aligned with magnetic structure may then be construed from an ordered set of such sets. Now formally since $\psi = \psi(R,\zeta)$ in any poloidal cross-section, each flux surface having constant $\psi_j$ may be depicted by functions $R(\zeta,\psi_j)$ or $\zeta(R,\psi_j)$, which in general will be multi-valued. For a single-null divertor, $R(\zeta,\psi_j)$ in particular will be double-valued everywhere except where $(\partial R/\partial\zeta)\big|_{\psi_j} \to \infty$, where lower $\zeta$ values are reached in either inner or outer divertor chamber, and at the degenerate points of magnetic axis and poloidal field singularity. Also, data matrices of $\psi$ values available from completed HF calculations relate to regular rectangular lattices in $R,\zeta$ co-ordinates. One could envisage primarily obtaining $(R_i,\zeta_i)$ pairs at fixed $\psi_j$ by scanning a matrix from HF along each row of constant $\zeta$ and locating both intercepts with the $\psi_j$ contour.

In single-null configurations, flux surfaces to be interpolated are divisible into three categories: those of (a) open scrape-off layer, (b) closed main torus and (c) open divertor private region types. We evaluate them in this order. Although as suggested, pairs of points on a contour $\psi_j$ may be determined by scanning poloidal flux function data along each horizontal row, this is obviously acceptable only while $(\partial R/\partial\zeta)\big|_{\psi_j}$ remains of order one or less. At some point, such a constraint may be violated and one must switch to analagous interpolation along columns of constant R, taking care to ensure a smooth match between zones. So for scrape-off layer surfaces, vertical interpolation is required around their tops. Presently, explicit gradients are not examined, but rather a transition to searching along major radial chords is made simply when the smaller major radius side of a contour exceeds a certain bound and simultaneously lies higher than the magnetic axis. Similarly for main torus surfaces, an equivalent process is applied both to their tops and bottoms, intersection of another pre-set bound again controlling. These two bounds are connected respectively to the magnetic axis and X-point chords by a single loose input parameter. Divertor private flux surfaces are always interpolated vertically.

Using a formula like linear interpolation, for which inferred values are bounded above and below by end-points $\psi^{[k]}$, $\psi^{[k+1]}$, lattice intervals k along either a row or column where a selected function value $\psi_j$ is crossed are of course readily distinguished by a condition*:-

$$\psi_j \in [\psi^{[k]}, \psi^{[k+1]}] \Rightarrow (\psi_j - \psi^{[k]})(\psi_j - \psi^{[k+1]}) \leq 0. \qquad (20)$$

In the present context, poloidal plane co-ordinates $R, \zeta$ may also be regarded as Cartesian (i.e. unit plane metric), so a general intermediate position $\chi$ where $\psi_j$ is achieved may be located just by a standard linear expression:-

$$\chi = \frac{(\psi_j - \psi^{[k]})\chi^{[k+1]} + (\psi^{[k+1]} - \psi_j)\chi^{[k]}}{(\psi^{[k+1]} - \psi^{[k]})} . \qquad (21)$$

A set of flux surfaces $\{\psi_j\}_j$ thus to be interpolated is determined according to whatever spatial discretisation is desired, since of course they constitute boundaries defining transformed grid rows. Arbitrary grid distributions in flux surface orthogonal dimension $\sigma_y$ are currently imposed with respect to the separatrix. This critical surface is interpolated first‡, its characteristic poloidal flux $\psi_S$ also being furnished by HF. Scrape-off layer surfaces are disposed within an interval extending from the separatrix point of maximum major radius, expecting it to approximate closely the position of minimum scrape-off thickness. This is normalised, to H say, by an input parameter. Inside the separatrix a precisely reflected distribution is assumed, but here over an interval a parameterised fraction of H in thickness. Grid rows are arranged within these intervals by a normalised function implying their proportional spatial extents. Currently a single parameter form providing for greater resolution around the separatrix, in anticipation of plasma behaviour, is employed:-

---

* A certain machine dependence in this criterion was discovered. On CRAY-1S and -XMP mainframes, real variable word lengths are sufficient to detect exact coincidences with end-points, when (20) vanishes. Care is then needed to prevent double counting of an intercept, from lattice intervals on either side of the end-point. On a PRIME, due to its shorter word length these coincidences are apparently not found, and no repetition occurs.

‡ Another small machine dependence emerged. A divertor X-point occurs as a single lattice point in HF magnetic flux data, and hence is again exactly picked out by CRAY processors but not by a PRIME. Numbers of separatrix co-ordinates $(R_i, \zeta_i)$ thus differ by one in each environment, affecting their subsequent ordering algorithms. For PRIME, a null-point position is estimated as where the two appropriate separatrix straight-line segments intersect.

$$f_y(0\leq\omega\leq 1) = \omega\{\gamma+(1-\gamma)\omega\} \;;\; (0\leq\gamma\leq 1). \qquad (22)$$

Once flux function values $\{\psi_j\}$ at each location are deduced, according to an inversion of linear form (21), they are subsequently interpolated around the structure as described before. In fact, mid-surfaces representing lines through grid row centres are also required, and they are constructed as well.

Divertor private region surfaces are treated slightly differently. An outermost flux value $\psi_0$ is identified as that obtaining at a position $(R_0,\zeta_0)$ a parameterised distance vertically below the X-point. Adherence to piecewise linear interpolation is still maintained by applying a bilinear formula involving its four surrounding lattice points, $\psi_{k\ell};\psi_{k+1\ell};\psi_{k\ell+1};$ $\psi_{k+1\ell+1}$ with $\psi_{k\ell} \equiv \psi(R_k,\zeta_\ell)$ etc, viz:-

$$\psi_0 = (1-\lambda_R)(1-\lambda_\zeta)\psi_{k\ell} + \lambda_R(1-\lambda_\zeta)\psi_{k+1\ell} + \lambda_\zeta(1-\lambda_R)\psi_{k\ell+1} + \lambda_R\lambda_\zeta\psi_{k+1\ell+1} \;; \qquad (23)$$

$$\lambda_R = \frac{R_0-R_k}{R_{k+1}-R_k} \;;\; \lambda_\zeta = \frac{\zeta_0-\zeta_\ell}{\zeta_{\ell+1}-\zeta_\ell} \,.$$

A straight line projected through magnetic axis and X-point is temporarily taken roughly to represent a magnetic flux orthogonal surface, and proportional distances along it between X-point and innermost contour are computed for each chosen main torus flux surface*. Additional divertor private flux contours are now distinguished, using bilinear approximation after (23), at points along this line in equal proportions between X-point and intersection with $\psi_0$. As remarked above, resulting contours, and mid-surfaces too, are then interpolated purely along major radial chords. Distributing flux surfaces in such a manner helps in procuring a smoother overall BRAAMS grid, as exemplified below.

Finally, having obtained sets of co-ordinates $\{(R_i,\zeta_i)\}$ for each $\psi_j$ outline, they must be ordered so that when traversed in sequence a directed locus around it is described. This ordering process is facilitated by a curve regarded as $R(\zeta,\psi_j)$ being <u>double-valued</u>, as referred to earlier. Hence by scanning HF data along ascending rows of fixed $\zeta$ co-ordinates are generated in correlated pairs. In NET-3A, lower $\zeta$ values are attained in its outer divertor arm, so a few leading points occurring singly for each

---

* It is important to recall that hereafter, by intersection with a magnetic flux surface we explicitly intend an intercept with a constituent straight-line segment in its approximate representation. Thus neighbouring points $(R_i,\zeta_i)$; $(R_{i+1},\zeta_{i+1})$ straddling a straight line connecting $(R_1,\zeta_1)$; $(R_2,\zeta_2)$ are disclosed by a condition:-

$$[(R_2-R_1)\zeta_i+(R_i-R_2)\zeta_1+(R_1-R_i)\zeta_2]\;[(R_2-R_1)\zeta_{i+1}+(R_{i+1}-R_2)\zeta_1+(R_1-R_{i+1})\zeta_2] \leq 0 \;;$$

$$(\zeta_2\neq\zeta_1), \qquad (24)$$

and their actual enclosed point in common is found as described for two crossing straight lines in sub-section 3.3.

scrape-off surface are discriminated by finding the first large proportional change in $(\partial R/\partial \zeta)\big|_{\psi_j}$ between succeeding points. Thereafter, correct ordering is attained by registering alternate points over increasing $\zeta$, next continuously those co-ordinates interpolated vertically around their tops, and lastly the intervening points over decreasing $\zeta$. Closed main torus surfaces are ordered employing a similar approach, starting and ending at intersections with the magnetic axis to X-point straight line. Divertor private region contours are ordered automatically in scanning along progressive columns of fixed R.

In practice, an extra difficulty tends to arise owing to plasma grid spacings demanded typically being small compared with poloidal plane resolutions of HF data. Around the X-point, main torus and divertor private flux surfaces and separatrix are interpolated in orthogonal directions, i.e. vertically and horizontally respectively. Unmatching errors in small scale interpolation can then lead to some fallacious contour crossings. To conclude, points on former region mid-surfaces adjacent to the separatrix are refined near the X-point by ascertaining, using an adaptation of (20) over azimuthal co-ordinates $\zeta_i$, that they lie between separatrix and next contours of increasing $\psi$. If initially they do not, they are repositioned as in (21) to new $\zeta_i$ in proportion to their intermediate magnetic flux values. An example of a completed set of organised piecewise linear flux surfaces is illustrated for NET-3A in FIG. 2, taking minimum scrape-off layer thickness H=10 cm, corresponding main torus width 16 cm, and divertor vertical depth below X-point 65 cm.

### 3.3 Orthogonal Surfaces

As stated previously, BRAAMS calculations must be executed in an orthogonal co-ordinate frame, and so for both along field and poloidal versions their second essential co-ordinate $\sigma_y$ must everywhere be orthogonal to magnetic flux surfaces, i.e. parallel to $\nabla\psi$. Naturally, this is beneficial computationally also in being aligned with cross-field transport. Having constructed constant flux contours $\{\psi_j\}_j$ as above, one must now infer a set of normal curves, consistent again in a piecewise linear sense and corresponding in turn to a requested distribution of transformed grid column boundaries. Their intersections with $\{\psi_j\}$, in other words, comprise the vertices of each cell in a magnetically oriented discrete solution space. Associated metric functions may immediately be extracted from such a spatial net.

Considering an arbitrary position P on a piecewise linear flux surface $\psi_j$, basically we wish to determine the straight-line segment connecting it to the next such contour $\psi_{j-1}$;$\psi_{j+1}$ which best approximates an intervening orthogonal co-ordinate arc. Ordered sequences of these segments then produce equivalent piecewise linear orthogonal surfaces. There are several ways in which one could envisage estimating an individual element. Most simply, one might project a perpendicular to the $\psi_j$ segment through P to its intercept P' with $\psi_{j-1}$ or $\psi_{j+1}$. However, although this line would subtend a right-angle at P, it would in general meet $\psi_{j-1}$ or $\psi_{j+1}$ segments at quite an arbitrary angle at P'. A curve composed of these elements would tend systematically to depart from actual orthogonal ones of consistent curvature, or at worst may become excessively jagged. Clearly, an obvious compromise is to make some allowance for surface curvatures by not biassing an element with one of its ends only; a line should be projected from P so as to subtend <u>equal</u> angles with flux contour segments at P and P'. Three lines thus conjoined form the base of an isosceles triangle.

It will be appreciated that such a method makes no reference expressly to data concerning $\nabla\psi$. Superficially, it may be thought advantageous to utilise this information. For a perfectly axisymmetric system, $\nabla\psi$ at any point in a poloidal cross-section is parallel to a line having Cartesian gradient:-

$$\left(\frac{\partial\psi}{\partial\zeta}\right) \Big/ \left(\frac{\partial\psi}{\partial R}\right). \tag{25}$$

One could therefore estimate each derivative, for example by some finite difference approximation, over an HF flux function matrix, interpolate them to position P, and obtain there a local direction of $\nabla\psi$. But then one relies on two interpolations of two interpolated derivatives, a process which becomes of questionable accuracy since grid spacings small compared with HF resolutions, as alluded to before, are commonly involved. Again, the situation may be thought to be partially improved if HF calculations were repeated and made themselves to furnish more precise information on $\nabla\psi$ at every lattice point. However, in both cases a more serious criticism still applies. Each straight-line segment in a piecewise linear flux contour will in general not be tangential to the exact flux surface actually passing through a point P anywhere along its length, including its ends. Hence a line projected from P, even if exactly parallel to $\nabla\psi$ there, typically will subtend some angle different from $\pi/2$ with its original flux segment. Furthermore, it will meet a segment on a neighbouring contour at another arbitrary angle, unrelated to local $\nabla\psi$. Just like simple perpendiculars discussed above, a chain of such elements might correspond to a rather ragged orthogonal surface. Modifying an element to take into account $\nabla\psi$ also at its sought end-point P', which consequently would have to be iterated on, would merely recover an analogue of our suggested isosceles technique. Thus as regards generating orthogonal surfaces of maximum consistency with magnetic flux surfaces already determined, and all piecewise linear, the isosceles approach should be at least as good as other fits directly involving flux gradient details.

With this purely geometric method, finding end-points of isosceles line elements in a given orthogonal curve can be framed entirely in terms of intersections of two straight lines joining points $(R_1,\zeta_1);(R_2,\zeta_2)$ and $(R_3,\zeta_3);(R_4,\zeta_4)$ respectively. Now if they cross at $(R_I,\zeta_I)$ we have:-

$$\begin{aligned} R_I &= \frac{(R_1\zeta_2-R_2\zeta_1)(R_4-R_3)-(R_3\zeta_4-R_4\zeta_3)(R_2-R_1)}{(\zeta_2-\zeta_1)(R_4-R_3)-(\zeta_4-\zeta_3)(R_2-R_1)}\ ; \\ \zeta_I &= \frac{(R_1\zeta_2-R_2\zeta_1)(\zeta_4-\zeta_3)-(R_3\zeta_4-R_4\zeta_3)(\zeta_2-\zeta_1)}{(\zeta_2-\zeta_1)(R_4-R_3)-(\zeta_4-\zeta_3)(R_2-R_1)}\ , \end{aligned} \tag{26}$$

while they are parallel if:-

$$(\zeta_2-\zeta_1)(R_4-R_3)-(\zeta_4-\zeta_3)(R_2-R_1) = 0. \tag{27}$$

Suppose on adjacent flux contours $\psi_j$ and $\psi_{j-1}$ or $\psi_{j+1}$ we have identified particular segments between respective co-ordinates $(R_i^{[j]},\zeta_i^{[j]})$; $(R_{i+1}^{[j]},\zeta_{i+1}^{[j]})$ and $(R_n^{[j\pm1]},\zeta_n^{[j\pm1]})$; $(R_{n+1}^{[j\pm1]},\zeta_{n+1}^{[j\pm1]})$. Here one difficulty is given segment index i, to find an appropriate segment index n, since flux surfaces generally consist of distinct numbers of components not necessarily spatially cross-correlated. Already having ordered them into series, though, we examine a small range of $\psi_{j-1};\psi_{j+1}$ components on either side of one with an initial end-point closest to $(R_i^{[j]},\zeta_i^{[j]})$. In each instance, if when extended segments i and n share a common point $(R_I,\zeta_I)$ according to (26), its distance from starting point P on $\psi_j$ is computed. Both points P'; P" along extended $\psi_{j-1};\psi_{j+1}$ segment n an equal distance from $(R_I,\zeta_I)$ are established, and either or both lying within $(R_n^{[j\pm1]},\zeta_n^{[j\pm1]})$ to $(R_{n+1}^{[j\pm1]},\zeta_{n+1}^{[j\pm1]})$ counted as potential next orthogonal element end-points. If on the other hand, segments i and n satisfy (27) and are parallel, a perpendicular to line i is projected from P, denoted $(R_o,\zeta_o)$, its intercept $(R_p,\zeta_p)$ along extended component n being given by:-

$$R_p = \frac{(R_4-R_3)(\zeta_2-\zeta_1)\zeta_o+(R_4-R_3)(R_2-R_1)R_o+(R_4\zeta_3-R_3\zeta_4)(\zeta_2-\zeta_1)}{(\zeta_2-\zeta_1)(\zeta_4-\zeta_3)+(R_2-R_1)(R_4-R_3)} ;$$
$$\zeta_p = \frac{(\zeta_4-\zeta_3)(\zeta_2-\zeta_1)\zeta_o+(\zeta_4-\zeta_3)(R_2-R_1)R_o-(R_4\zeta_3-R_3\zeta_4)(R_2-R_1)}{(\zeta_2-\zeta_1)(\zeta_4-\zeta_3)+(R_2-R_1)(R_4-R_3)} . \qquad (28)$$

This is alternatively counted as a potential orthogonal end-point should it be contained between $(R_n^{[j\pm1]},\zeta_n^{[j\pm1]})$ to $(R_{n+1}^{[j\pm1]},\zeta_{n+1}^{[j\pm1]})$.

For both circumstances, it was found necessary further to restrict potential next end-points by rejecting those which implied a greater than specified change in gradient between successive orthogonal line elements. Letting $(R_<,\zeta_<);(R_o,\zeta_o)$ be the two preceding element end-points on flux contours $\psi_{j+1};\psi_{j-1}$ and $\psi_j$ (at P), and $(R_>,\zeta_>)$ the putative continuation (at P'), we additionally insist that:-

$$(1-\beta)[(R_o-R_<)(R_>-R_o)+(\zeta_o-\zeta_<)(\zeta_>-\zeta_o)]^2-\beta[(R_o-R_<)(\zeta_>-\zeta_o)-(R_>-R_o)(\zeta_o-\zeta_<)]^2 \geq 0, \qquad (29)$$

where $\sqrt{\beta}$ is cosine of a parametric largest angle permitted at P. Lastly, extra care is required in all contingencies when $R_{n+1}^{[j\pm1]} = R_n^{[j\pm1]}$ in order to accommodate infinite $(\partial\zeta/\partial R)\big|_{\psi_{j\pm1}}$ along flux component n.

Following this procedure, as remarked, for a small number of segments on flux contour $\psi_{j-1};\psi_{j+1}$, a number N of possible new locations P' are accrued. Normally it is sufficient merely to select from these whichever is closest to P. However, if N=0 we again seek perpendicular intercepts as in (28) on those components n not parallel to segment i, choosing finally whichever of these or of sectional co-ordinates $(R_n^{[j\pm1]},\zeta_n^{[j\pm1]})$ themselves is closest to P. Ultimately, an unambiguous step P' and consequent orthogonal line element are obtained.

The LINDA geometry interpolation code thus has at its heart a routine which, beginning either on a peripheral magnetic flux surface or separatrix, produces an approximate orthogonal surface employing a piecewise linear sequence of isosceles steps. In fact, having flux mid-surfaces available, these are also used initially in a sequence, before reallocating a mid-point on each cell orthogonal face where a straight line connecting its vertices then intersects their enclosed mid-surface (see FIG.11). An isosceles algorithm as described appeared adequately to encompass all discretised flux surface contingencies encountered in the single-null divertor problem examined.

There remains just one critical orthogonal curve which cannot be ascertained as above, namely one exactly passing through the poloidal magnetic field singularity. If orthogonal surfaces are instituted from separatrix points equal distances $ds_x^p$ on either side of the X-point, they stay distinct and well defined as $ds_x^p$ is decreased until a certain threshold value is reached, when they tend to cross. In effect, minimum $ds_x^p$ reflects a limit on resolution attendant on the finite accuracy of piecewise linear representation of magnetic flux surfaces; this is of course least reliable where curvatures become extreme close to $B_\theta \to 0$. To approximate an X-point coincident curve we therefore take those orthogonal surfaces starting just outside minimum $ds_x^p$ and derive their mid-position on a peripheral flux surface. An orthogonal curve is projected back in from there to within a few flux contours of the X-point. Finally, it is joined to it by a continuous straight line, thereby averting a deviation ultimately to one side because of inaccuracies.

Where orthogonal surfaces are placed is again a matter of choice regarding a plasma grid. To ensure a certain level of geometric authenticity, we fix permanently particular orthogonal boundaries, while all others may be arbitrarily deployed. Hence we always include those surfaces passing through positions of (i) target and separatrix intersections, (ii) X-point, and (iii) minimum major radius, (iv) maximum elevation ($\zeta$) and (v) maximum major radius on torus scrape-off outermost flux surface. Note (i) may be determined either according to specified major radii or separatrix distances from (i) to (ii). For a single-null divertor, six sectors are defined. In inner and outer divertor chambers (i) to (ii) parametric numbers of grid columns are inserted, and the remainder divided between torus regions (ii) to (iii), (iii) to (iv), (iv) to (v) and (v) to (ii) in proportion to their respective separatrix arc lengths biassed by a set of input parameters. Within each separate sector, a resulting number of orthogonal boundaries are disposed at separatrix intervals again in proportion to some normalised function. Currently grid columns are clustered in anticipation of plasma characteristics by exercising in main torus regions, either over a whole sector or symmetrically over its two halves, a single parameter logarithmic form:-

$$f_x^I(0\leq\omega\leq 1) = 1 - \frac{\ell n(1+\gamma-\gamma\omega)}{\ell n(1+\gamma)} \; ; \; (\gamma>0). \qquad (30)$$

An alternative form for divertor chambers has been tailored to expected ranges of recycled neutral particles, giving before a target two grid columns each of order 1 cm in width, i.e:-

$$f_x^{II}(0\leq\omega\leq 1) = \frac{\omega^\gamma}{41}\left\{5 + 4(4\omega-1)^2\right\} \; ; \; (\gamma>0). \qquad (31)$$

In fact, as previously with flux contours, orthogonal mid-surfaces are also developed, being initiated from median positions of each separatrix interval relating to a grid column. Mid-points on cell faces parallel to magnetic flux surfaces are assigned where a straight line between vertices intersects their orthogonal mid-surface (see FIG.11). Due to concavity of flux contours, however, some linear parallel faces may clearly lie outside the range of interpolated orthogonal mid-curves, which always end on flux segments themselves. When this occurs, a face mid-point is assumed at its intersection with an extrapolation of the last available orthogonal line element. Lastly, although flux mid-contours are still exploited in deducing orthogonal mid-curves, cell centres are situated for consistency at the crossing points of straight lines joining each pair of mid-points on their flux parallel and orthogonal faces (see FIG.11).

Completed flux normal co-ordinates are arranged in order from either outermost divertor private, or innermost main torus, flux surfaces to outermost scrape-off layer one. A set of piecewise linear orthogonal surfaces, accompanying that of magnetic flux surfaces introduced above, is also shown for NET-3A in FIG.2. Furthermore, the actual discrete grid formed by taking their intersections as vertices of quadrilateral mesh cells is depicted, along with their corresponding centres. As called for, we have in an orthogonal frame a solution space discretisation everywhere closely aligned with toroidally symmetric magnetic geometry. At this stage, LINDA produces an output file specifying all grid points in poloidal plane co-ordinates $(R,\zeta)$. For every cell its nine fundamental points, as detailed in FIG.11, are listed, beginning on the inner divertor target at its outermost private flux zone, proceeding along that row to its outer target end, and continuing thus row by row towards the scrape-off outer edge. Such a grid description is generally suitable for supplying a precisely equivalent geometry eventually to Monte Carlo neutral particle simulation codes[5,6].

There is one prominent disadvantage of orthogonal co-ordinates implicit in our discussion above and made manifest in FIG.2. One is constrained to accept orthogonal surfaces as boundaries to a solution region at which one wishes to impose conditions representing, for example, plasma incidence onto material targets. In other words, BRAAMS can model directly only targets orthogonal to magnetic flux surfaces. This is a significant deficiency with regard to divertors in large tokamaks, of course, since it is essential that their targets be inclined at a very shallow angle to magnetic field lines in order to avoid intolerably dense power depositions. A marked obliquity to poloidal flux surfaces is included. Means to circumvent or accommodate such a discrepancy in BRAAMS simulations have been actively pursued, but ultimately only a new code both allowing its equations to be framed, and capable of solving them numerically, in a non-orthogonal co-ordinate system would overcome it fully. Presently, calculations incorporating a complete poloidal cross-section through a device, like FIG.2, must concede orthogonal targets, with a possibility subsequently of applying some physically based transformation to their results. Note a further connotation due to convergence of magnetic flux surfaces, again exemplified in FIG.2, is an inability in general also to model plane divertor plates.

### 3.4 Metric Functions

Once an orthogonal discretisation of magnetic geometry has been derived, its characteristics must be encoded into those metric functions employed in BRAAMS to define its solution space. Recollect these are cell by cell diameters $ds_x$;$ds_y$, interfacial areas $a_x$;$a_y$ and volumes V. With poloidal cross-section co-ordinates, magnetic field pitch information ($B_\theta/B$) is also required. Like cell vertex co-ordinates above, quantities are listed in an order applying to BRAAMS grids; from inner target to outer target along each row, stepping from innermost flux surfaces to outermost scrape-off layer ones, in a single-null divertor configuration.

One major discrepancy remains in such a geometric treatment. It is obvious that a nominally rectangular computational domain and divertor magnetic flux surfaces are topologically distinct, i.e. there is no homeomorphic transformation mapping one into the other. Compatibility can only be achieved if the computational grid is rendered discontinuous, a property accomplished by introducing cuts. These special columns of cells isolate one grid sector from an adjacent one, typically by invoking zero coefficients to make a wholly impenetrable barrier to all transport. We insert two cuts extending from innermost flux surfaces to separatrix, and dividing the lower half of a grid into single-null divertor private, and inner main torus, flux regions. Closed inner contours are disposed between cuts, starting and ending on that magnetic flux orthogonal surface passing through the X-point. Divertor private zones from inner target to this continued orthogonal surface, and from there to outer target, are assigned respectively to those grid sectors to left and right outside the cuts. Hence proceeding along one of these lower grid rows, from inner target one follows a divertor private magnetic flux tube up to a cut, then leaps to its main torus counterpart an equal number of grid rows from the separatrix, encircles this to a second cut, jumps back to the original private flux tube, and concludes up to outer target. Scrape-off layer surfaces simply map continuously to upper grid rows.

Now left-hand cut right edge plus right-hand cut left edge, and left-hand cut left edge plus right-hand cut right edge, physically are continuous, being respectively associated sides of X-point coincident orthogonal curves over main torus and divertor private flux surfaces. To facilitate special action on interior boundaries so as to express physical continuity we construct each cut from three columns of cells. A central insulating column, as already mentioned, is sandwiched between two providing for appropriate cross-matching of plasma features. It is emphasised that cut cell columns are a purely numerical device without geometric relevance. To this end, they are attributed zero longitudinal width $ds_x$ in LINDA, it being incumbent on subsequent exploitations to recalibrate them as necessary.

For a poloidal co-ordinate frame, cell widths $ds_x^P$;$ds_y^P$ are suitably represented by respective face mid-point to face mid-point Cartesian distances 5 to 6 and 7 to 8 (see FIG.11). Projections of these dimensions for NET-3A discretised as in FIG.2 are shown in FIG.3 and FIG.4. Each is plotted over computational grid indices ordered as discussed according to BRAAMS convention. We reiterate lower grid rows step between divertor private and inner main torus regions across the cuts, which are themselves plainly visible as zero value gullies in $ds_x^P$ (FIG.3). Similarly, large spikes in $ds_y^P$ occurring inside the cuts (FIG.4) are not important since

special treatment of these columns in BRAAMS calculations is anyway understood. Also inset in FIG.3 is total length along each grid row as a function of its initial face mid-position (5) on the inner target, relative to outermost private flux surface. Note there is very little variation (~5%) in poloidal arc length of each scrape-off flux tube. A corresponding total width exterior and interior to separatrix across each grid column is inset in FIG.4, against separatrix distance from inner target. Our input minimum scrape-off thickness of 10 cm is evident here.

Remaining metric functions emerge from our previous model of ignorable co-ordinate extent $\Delta s_z^P$. We employ a tube of fixed poloidal magnetic flux condition (14), taking normalisations for all grid rows at inner target to be unity $\Delta s_z^P(0,\sigma_y^P) = 1$ m. In fact, as hinted in sub-section 2.2, a more proper identification for each poloidal plane element in a toroidally symmetric structure would be $\Delta s_z^P(0,\sigma_y^P) = 2\pi R(0,\sigma_y^P)$, its circumference of revolution about the centre line. Note using (12) this would imply in along field co-ordinates a uniformity direction normalisation of $\Delta s_z^F(0,\sigma_y^F) = 2\pi R(0,\sigma_y^F)\, B_\theta(0,\sigma_y^F)/B(0,\sigma_y^F)$, which closely resembles division of surface area of a circular cross-section tokamak having minor and magnetic axis major radii $a, R_A$ respectively into a rational flux tube:-

$$\frac{S}{L} \approx \frac{4\pi^2 a R_A}{2\pi R_A q} = 2\pi R_A \frac{B_\theta}{B_\phi} . \qquad (32)$$

However, unit normalisation for every row in a poloidal cross-section leads to little error certainly for NET-3A, where fractional variation in major radius across the inner target is marginal (<10%). To enforce (14), scalar poloidal magnetic induction at any point is estimated from companion HF data regarding cotangent of magnetic field line pitch angle $t \equiv (B_\theta/B_\phi)$ and a standard toroidal field formula, viz:-

$$B_\phi = \text{constant}. \frac{1}{R} \Rightarrow \frac{B_\theta(0,\sigma_y^P)}{B_\theta(\sigma_x^P,\sigma_y^P)} = \frac{t(0,\sigma_y^P)}{t(\sigma_x^P,\sigma_y^P)} \frac{R(\sigma_x^P,\sigma_y^P)}{R(0,\sigma_y^P)} . \qquad (33)$$

Consistent pitch data from HF are of course arranged over the same spatial lattice as poloidal flux function data, and to maintain piecewise linear approximation once more we interpolate them to any location according to a bilinear form after (23).

Interfacial areas between cells along a grid row $a_x^P = ds_y^P \Delta s_z^P$ (cf (6)) are computed as a product of orthogonal width between vertices 1 to 3 on inner target and 2 to 4 thereafter with toroidal extent evaluated at respective mid-points 5 and 6 (see FIG.11). Resulting areas again for NET-3A discretisation FIG.2 are projected over grid indices in FIG.5, with column sums either side of separatrix inset against separatrix distance from inner target. Normal interfacial areas along a grid column $a_y^P = ds_x^P \Delta s_z^P$ are likewise inferred from cell width between vertices 1 to 2 on innermost magnetic flux surfaces and 3 to 4 elsewhere multiplied by toroidal extent centrally across that cell, i.e. calculated at centre 9 (see FIG.11). Our equivalent NET-3A grid projection is depicted in FIG.6, together with grid row total versus initial position on inner target.

A significant question here is treatment of toroidal normalisations across grid cuts. While (14) determines $\Delta s_z^P(\sigma_x^P, \sigma_y^P)$ uniquely everywhere in divertor private and scrape-off regions given inner target values $\Delta s_z^P(0, \sigma_y^P)$, in traversing a grid cut one enters onto a new main torus poloidal flux tube. As before, $\Delta s_z^P$ could unambiguously be reset by equating it to $2\pi R$, but we presently use an alternative strategy. Normalisations for each lower half grid row are multiplied by a factor when crossing to main torus cells, firstly incorporating its proportional discontinuity in $B_\theta$ and secondly such that there is a smoother transition in total interfacial area between those rows bordering the separatrix. In effect, considering a total area graph resembling FIG.6, inner main torus contributions are scaled until least square straight lines through parameterised numbers of row values inside and outside the separatrix intersect on it*. Both separatrix contiguous rows are also brought exactly onto these lines by applying extra factors, in the scrape-off to its initial normalisation $\Delta s_z^P(0, \sigma_y^P)$ which consequently is increased fractionally above unity. This further improves smoothness of critical area change onto open magnetic flux surfaces.

Cell volumes $V^P = ds_x^P ds_y^P \Delta s_z^P$ are estimated from our previous diametric measures between face mid-points 5 to 6 and 7 to 8, and ignorable co-ordinate width again at centre 9 (see FIG.11). Thus one most naturally approximates a logical principle that cell to cell interfacial areas should be simple interpolations of centre based volumes and lengths. Projection over grid indices for our illustration NET-3A discretisation is presented in FIG.7, zero value $\sigma_y^P$ - direction channels still indicating the cuts. It will be observed we obtain substantial complexity, in conjunction, owing to clustering of mesh lines simultaneously around separatrix and targets and spreading in torus boundary regions of low curvature, with extreme variations in magnitude. Recall from (6) that FIG.7 essentially refers to (one over) the Jacobian for orthogonal transformation to this physical solution space.

---

* Consider a set of N Cartesian points $\{(x_i, y_{Ai}+\lambda y_{Bi})\}_i$. Let:-

$$\mu_1 \equiv \sum_{i=1}^{i=N} x_i \; ; \; \mu_2 \equiv \sum_{i=1}^{i=N} x_i^2 \; ; \; \mu_3 \equiv \sum_{i=1}^{i=N} x_i y_{Ai} \; ; \; \mu_4 \equiv \sum_{i=1}^{i=N} x_i y_{Bi} \; ;$$
$$\mu_5 \equiv \sum_{i=1}^{i=N} y_{Ai} \; ; \; \mu_6 \equiv \sum_{i=1}^{i=N} y_{Bi} . \qquad (34)$$

A least squares straight line fit may be written $y = \alpha x + \beta$, where:-

$$\alpha = \frac{(\mu_1\mu_5 - N\mu_3) + (\mu_1\mu_6 - N\mu_4)\lambda}{\mu_1^2 - N\mu_2} \; ; \; \beta = \frac{(\mu_1\mu_3 - \mu_2\mu_5) + (\mu_1\mu_4 - \mu_2\mu_6)\lambda}{\mu_1^2 - N\mu_2} . \qquad (35)$$

If in addition this fitted line must pass through an extra designated point $(x_I, y_I)$ then:-

$$\lambda = \frac{(\mu_1^2 - N\mu_2)y_I - (\mu_1\mu_5 - N\mu_3)x_I - \mu_1\mu_3 + \mu_2\mu_5}{(\mu_1\mu_6 - N\mu_4)x_I + \mu_1\mu_4 - \mu_2\mu_6} . \qquad (36)$$

In an along field co-ordinate system, we recollect from sub-section 2.2 only longitudinal dimension $ds_x^F$ and magnetic flux orthogonal area $a_x^F$ differ from poloidal frame metric functions, normal widths $ds_y$, areas $a_y$ and volumes V being identical in both cases. Now within a magnetic flux surface of constant $\sigma_y$, equation (10) yields:-

$$ds_x^F = ds_x^P \left(\frac{1}{ds_x^P}\int_0^{ds_x^P} \frac{B}{B_\theta}\, ds_x^P\right) = \int_0^{ds_x^P} \frac{\sqrt{1+t^2}}{t}\, ds_x^P, \qquad (37)$$

where $t \equiv (B_\theta/B_\phi)$ is local pitch information generated by HF. We solve this integral once more in a spirit of universal piecewise linear approximation, by allowing t to vary linearly along a flux contour straight line segment connecting two points $s_{xA}^P; s_{xB}^P$ in the poloidal plane, i.e:-

$$t = t_A + (t_B - t_A)\frac{(s_x^P - s_{xA}^P)}{(s_{xB}^P - s_{xA}^P)} \Rightarrow dt = \frac{t_B - t_A}{s_{xB}^P - s_{xA}^P}\, ds_x^P \Rightarrow ds_x^F = \frac{s_{xB}^P - s_{xA}^P}{t_B - t_A}\int_{t_A}^{t_B} \frac{\sqrt{1+t^2}}{t}\, dt. \qquad (38)$$

Substituting $r^2 = (1+t^2)$ one readily finds:-

$$ds_x^F = \frac{s_{xB}^P - s_{xA}^P}{t_B - t_A}\left\{ \sqrt{1+t_B^2} + \frac{1}{2}\,\ell n\left(\frac{\sqrt{1+t_B^2}-1}{\sqrt{1+t_B^2}+1}\right) - \sqrt{1+t_A^2} - \frac{1}{2}\,\ell n\left(\frac{\sqrt{1+t_A^2}-1}{\sqrt{1+t_A^2}+1}\right)\right\}, \qquad (39)$$

which also tends smoothly to the expected limit $(s_{xB}^P - s_{xA}^P)(B_A/B_{\theta A})$ when $t_B \to t_A$. To evaluate magnetic connection lengths $ds_x^F$ across grid cells, expression (39) is actually applied in just two steps roughly along their mid-surfaces; from face mid-point 5 to centre 9 to face mid-point 6 (see FIG.11), respective t values being interpolated bilinearly analagously to (23). Consequent extents for NET-3A study FIG.2 are shown over mesh indices in FIG.8, together with total grid row lengths against inner target intercept. Here one should contrast FIG.8 with FIG.3, noting in particular a very pronounced variation in scrape-off magnetic connection length from target to target (>50%). It is evident that much of this exaggerated shear is contributed just by those few cells very close to the X-point, for which $ds_x^F$ of course becomes greatly elongated. Everywhere else, shear through any grid column is mild to negligible. Magnetic shear is a very significant feature of authentic tokamak geometries, and is readdressed briefly in Section 4 below.

Along field cell to cell areas $a_x^F$ are immediately deduced from (12), giving:-

$$a_x^F = \frac{B_\theta}{B}\, a_x^P = \frac{t}{\sqrt{1+t^2}}\, a_x^P. \qquad (40)$$

Pitch t is calculated at face mid-point 5 on inner target and 6 elsewhere (see FIG.11). Corresponding areas over our NET-3A grid, plus column sums for scrape-off and inner regions, are displayed in FIG.9. Since each grid row is a tube of fixed magnetic flux (cf(9)), invoking a standard toroidal field relation we may note:-

$$a_x^F = \text{constant}. \frac{1}{B} \approx \text{constant}. R\left(\frac{1-t^2}{2}\right) \approx \text{constant}. R, \qquad (41)$$

or $a_x^F$ varies roughly as major radial co-ordinate. Comparing FIG.9 with FIG.2 affirms such an expectation.

Specification of magnetic geometry is completed[3] by coupling to other poloidal co-ordinates data cell centre values of $(B_\theta/B)$. To produce discretisations of maximum consistency we invert (11), ascribing to each cell a mean value equal to $ds_x^P(1/ds_x^F)$, where $ds_x^F$ derives according to (39) as explained. Only inside cuts and on the target boundaries* themselves do we set it explicitly to $(t/\sqrt{1+t^2})$. Taking FIG.3 and FIG.8 we obtain a pertinent NET-3A grid function shown in FIG.10. While gradients in pitch angle are strong along field lines, therefore, we see they are trivial against $\sigma_y$ except around the X-point. This validates in general our former neglect of $\sigma_y$-dependence when relating magnetic flux orthogonal areas in (12).

Two further output files are created by LINDA, containing cell by cell listings in BRAAMS conventional grid order of compatible metric functions for poloidal and along field reference frames. Magnetic pitch data also accompany the former. Engaging realistic divertor representations in BRAAMS calculations becomes a matter merely of reading in such a file, then redefining cut cell dimensions as necessary. One final discrete measure is also supplied, to enable results to be normalised to total power effluxes anticipated into the plasma edge in point from inner ignited regions. Summing cell face areas $a_y$ around a grid innermost magnetic flux surface and dividing by its surface area of complete toroidal revolution identifies what fraction is actually covered. Now if an element of length $d\ell$ on some plane curve C is rotated through a small angle $d\phi$ about a centre line, it sweeps out an area $R(\ell)d\ell d\phi$ where R is (major) radial co-ordinate of element $d\ell$. Thus an entire figure of toroidal revolution for C with total length L has an area:-

$$S = 2\pi \int_0^L R(\ell)d\ell. \qquad (42)$$

We make a trapezoidal estimate of this integral for the grid discretisation between cuts of an innermost main torus closed flux surface. Separate contributions between face points 1 to 7 and 7 to 2 (see FIG.11) are counted from each cell. If in poloidal co-ordinates toroidal extents $\Delta s_z^P$ were assigned to $2\pi R$, as already mentioned, the whole torus fraction covered would effectively be unity. However, with our scheme of unit normalisation across inner target and smooth inside to scrape-off areas, obviously only a part torus is included. For NET-3A case in FIG.2, a ratio of roughly 3% is obtained.

---

* These points are necessary to set appropriate sheath conditions for oblique plasma incidence in both co-ordinate versions of BRAAMS.

It will be appreciated from foregoing sample NET-3A results that a particular issue remaining in LINDA is that of noise. An especially clear example is provided by parallel areas $a_y$ in FIG.6. Some degree of noise is inevitable in any interpolation problem, and here certain expediencies allow it to be reduced. By choosing flux surfaces determining grid rows in a zone of high poloidal magnetic induction, it is generally unlikely that they will be compressed any closer together anywhere else. Similarly, disposing divertor private flux surfaces in reflected proportion to main torus contours assists in producing a relatively smoother grid over its lower half cuts. Closed inner flux surfaces themselves are incorporated only so that one has a boundary on which certain symmetry conditions with respect to electron and ion transport are well obeyed. Clearly, one would like this innermost contour to separatrix region as narrow as possible, both because preliminary convergence of BRAAMS calculations can proceed no faster than slow cross-field transport of particles and energy across it, and because approximations, notably currentless flow, inherent to the BRAAMS model become increasingly severe at smaller minor radii. Again, though, one compromises to avoid growing noise from interpolations excessively fine compared with original HF data resolutions. A typical parameterisation emerges as portrayed for NET-3A in FIG.2. To a lesser extent, a similar consideration applies to fixing private sector thickness below the X-point.

One drawback of piecewise linear interpolation is its liability to generate numerical noise due to errors in locating magnetic flux surface points. This situation is especially acute near the X-point, where not only are errors accentuated by large flux surface curvatures and difficulty in describing orthogonal curves, but also gradients of $(1/B_\theta)$ are enormous. Such errors picked up in our toroidal renormalisation method of crossing cuts may underlie apparently quite systematic noise between NET-3A main torus grid rows, exemplified in FIG.6. Hence, in addition to its incurring fewer interpolative operations, alternatively setting $\Delta s_z^P$ for each poloidal plane cell explicitly to $2\pi R$ may lead to smoother metric results. Never-the-less, noise cannot in any case be arbitrarily smoothed out if one is to preserve consistency of functions. One may smooth $a_y$, for instance, viewing it as an adjustment to inferred values of $B_\theta$, but only if corresponding amendments are also made to $a_x^P; a_x^F; V$ and with greatest difficulty to integral connection length $ds_x^F$. Again, one could not smooth poloidal co-ordinate dimensions $ds_x^P; ds_y^P$ without simultaneously altering every other geometric quantity, plus actual cell vertex positions $\{(R_k, \zeta_k)\}_k$ as well. We attempt to minimise noise wherever possible, but do not interfere with final representations.

### 3.5 Technical Details

Presently, LINDA contains ~2700 executable statements in FORTRAN 77 dialect. Ordered poloidal flux function and cotangent of pitch angle data from HF are read directly from two formatted ASCII files. Graphical summaries of grid discretisation and metric characteristics are produced using current versions of the Culham GHOST package[12]. Since it is globally a "once-through" non-iterative code, execution takes typically only 12-15 s of CPU time on a CRAY-1S or -XMP when encoded using its CFT77 optimising compiler. All control parameters are initialised in a single block data segment, and cell normalised distributions $f_x; f_y$ defined in two function routines. By maintaining a compiled object module library, only a trivial recompilation among these three parts, followed by relinking, is needed to implement a new case.

Now spatial lattices over which magnetic information is determined by HF usually comprise 15000-20000 points, while interpolated piecewise linear flux contours themselves may each contain 200-300 plane co-ordinate points. Many more are contributed by orthogonal surfaces, and ultimately nine separate positions (see FIG.11) with eight distinct geometric measures are accrued from every cell. Thus if all these data were stored concurrently, rather heavy demands for storage would be entailed. We avoid any such inconvenience by declaring four real and one integer named common blocks, all of minimal size and repeatedly reused in successive stages of a calculation. Temporary workfiles are then employed to pass required co-ordinates etc between stages, transfers further being exploited to accomplish relevant reorderings. In addition to principal output files containing cell vertex co-ordinates, grid metric descriptions in both poloidal and along field systems and graphics, any other workfile may also optionally be disposed. This provides an extra useful potential to furnish more primitive aspects, like approximate magnetic flux surfaces.

## 4. SUMMARY & APPLICATION

In order iteratively to increase internal consistency in numerical simulations of divertor tokamak edge plasmas, a means of supplying unified and realistic magnetic geometries to BRAAMS plasma and Monte Carlo neutral particle transport codes has been devised. Taking poloidal plane distributions of axisymmetric flux function and pitch angle computed by the HF magnetostatic equilibrium code, a new interpolation program LINDA produces spatial discretisations everywhere closely according with physical magnetic structures. Linear approximation methods are employed through-out. Piecewise linear magnetic flux surfaces are constructed, each ordered sequentially, disposed arbitrarily outside and proportionally inside the separatrix. Based on an original geometric approach of subtending isosceles angles at segments of consecutive contours, arbitrary arrangements of orthogonal surfaces are also deduced. Intersections determine vertices of discrete grid cells, presentable directly in plane co-ordinates to Monte Carlo neutral particle codes or encoded in fundamental metric functions to two-dimensional BRAAMS calculations. Cell diameters parallel and normal to flux surfaces are required, together with interfacial areas and volumes. Thus extents in an associated symmetry direction are implied, being consistently fixed by total and poloidal magnetic flux tube conditions respectively in field line aligned and poloidal reference frames. Ordered metric listings are prepared for both these implementations of BRAAMS. Magnetic pitch angle values must accompany poloidal data, and are specified by approximate connection length averages.

Employing such an authentic geometry in either version of BRAAMS departs from previous simplified divertor studies[7] naturally in matters of detail, but most significantly in one crucial physical respect. Latterly, reduced representations have prescribed zero shear against magnetic flux orthogonal co-ordinate, i.e. every cell in a computational grid column was appointed equal connection length[7]. Recalling example FIG.8 and even FIG.3 for NET-3A demonstrates a true variation. In fact, some limit on maximum shear may be apposite, for instance no flux surface should be placed closer than a mean poloidal Larmor diameter from an interpolated X-point, or other constraint expressing its practical imprecision. Our illustrative mesh FIG.2 probably at worst only marginally contradicts such a proposition. In any case, finite shear may potentially increase numerical difficulties affecting stability and/or convergence of BRAAMS utilisations, or even in unfavourable circumstances excite physical modes, for example of a Kelvin-Helmholtz like nature. One obvious possibility to lessen difficulties might be to start

from some prototype metric in which shear is artificially decreased by inventing a poloidal magnetic field giving pitch angle invariance with orthogonal co-ordinate. For example, $t \equiv (B_\theta/B_\phi)$ may be set by LINDA always to a scrape-off mid-value in each grid column. Beginning from a converged BRAAMS solution for this easier situation, one could then move to an exact solution through a progression of intermediate stages of mounting shear, converging from its predecessor to a new steady-state plasma at each one, and so never perturbing severely from equilibrium. At least in poloidal cross-section co-ordinates, consistent first-order adjustments to metric functions for a small change $dB_\theta$ in poloidal magnetic induction are immediately conferred by (6) and our choice of toroidal dimension (14), whence:-

$$\frac{da_x^P(\sigma_x^P,\sigma_y^P)}{a_x^P(\sigma_x^P,\sigma_y^P)} = \frac{da_y^P(\sigma_x^P,\sigma_y^P)}{a_y^P(\sigma_x^P,\sigma_y^P)} = \frac{dV^P(\sigma_x^P,\sigma_y^P)}{V^P(\sigma_x^P,\sigma_y^P)} \approx \frac{dB_\theta(0,\sigma_y^P)}{B_\theta(0,\sigma_y^P)} - \frac{dB_\theta(\sigma_x^P,\sigma_y^P)}{B_\theta(\sigma_x^P,\sigma_y^P)} \; . \qquad (43)$$

Increments $dB_\theta$ themselves are expressible in terms of point steps in pitch data $c \equiv (B_\theta/B)$ augmenting poloidal geometric quantities:-

$$c = \frac{t}{\sqrt{1+t^2}} \Rightarrow \frac{dB_\theta}{B_\theta} = \frac{dt}{t} = \frac{1}{1-c^2}\frac{dc}{c} \; . \qquad (44)$$

Development so far implicitly has applied to single-null poloidal divertor edges. Assuming BRAAMS plasmas can eventually be obtained for them, perhaps via an evolutionary approach as indicated, one must still recall a proper need to treat double-null configurations for NET. Extending our linear interpolation of magnetic geometries should be reasonably straight-forward, since of course identical basic elements are again involved. Piecewise linear magnetic flux surfaces can be assembled as before, although now no change in interpolation direction and a distinct ordering algorithm distinguishing torus inner and outer sides are likely to be required for scrape-off contours. Above all, the essential kernel routine approximating an orthogonal curve across some set of these surfaces retains its validity. Generally, only a reorganisation of component processes is implied, to embody a new conventional cell order with more grid cuts for the BRAAMS calculation mesh. A double-null case effectively is composed just of two juxtaposed single-null arrangements, so chiefly adaptation consists of duplicating and suitably resorting our former procedures. In addition, resembling commensurate reflection of main torus inner flux surfaces into divertor private ones before, some extra criteria may be added to minimise loss of smoothness between reassimilated grid regions neighbouring on a cut.

## ACKNOWLEDGEMENTS

Helpful suggestions regarding approximation of discrete orthogonal surfaces and consistent ignorable co-ordinate extents were provided by Dr J.G. Morgan. Further assistance with symmetric toroidal dimensions was given by Dr B.J. Braams and Dr C.M. Bishop. Many useful discussions were also held with M.F.A. Harrison. Magnetostatic equilibrium data from HF were supplied by Dr P.I.H. Cooke.

REFERENCES


1. B.J. BRAAMS Proceedings 11th European Conference on Controlled Fusion and Plasma Physics, Aachen, 1983.
Europhysics Conference Abstracts 7D-II (1983) 431.

B.J. BRAAMS, P.J. HARBOUR, M.F.A. HARRISON & J.G. MORGAN

J. Nuc. Mat. 121 (1984) 75.

2. B.J. BRAAMS, M.F.A. HARRISON, E.S. HOTSTON & J.G. MORGAN

Proceedings 10th International Conference on Plasma Physics and Controlled Nuclear Fusion Research, London, 1984 (IAEA-CN-44/E-II-5-3).
Nuc. Fus. Supp., IAEA, 2 (1985) 125.

3. B.J. BRAAMS Culham Laboratory Report CLM-P725 (Aug. 1984).

4. K. LACKNER Comp. Phys. Comm. 12 (1976) 33.

5. D. HEIFETZ, D. POST, M. PETRAVIC, J. WEISHEIT & G. BATEMAN

J. Comp. Phys. 46 (1982) 309.

6. E. CUPINI, A. DeMATTEIS & R. SIMONINI

NET Report No. 9, Euratom, EUR XII - 324/9 (1983)

7. M.F.A. HARRISON, E.S. HOTSTON & A. DeMATTEIS

NET Report No. 50, Euratom, EUR-FU/XII-361/86/50 (1985)

M.F.A. HARRISON & E.S. HOTSTON

European contributions to 13th Workshop, INTOR Phase IIA, Part 3 (EURFUBRU/XII-52/86/EDV10), March 1986.
Critical Issues, Impurity Control Appendix 1.
European contributions to 14th Workshop, INTOR Phase IIA, Part 3 (EURFUBRU/XII-52/86/EDV20), December 1986.
Critical Issues, Impurity Control Appendices 4 & 5.

8. S.V. PATANKAR "Numerical Heat Transfer and Fluid Flow".
(McGraw-Hill, New York, 1980).

9. S.I. BRAGINSKII

in "Reviews of Plasma Physics", Vol. 1,
ed. M.A. LEONTOVICH
(Consultants Bureau, New York, 1965).

10. G.A. KORN & T.M. KORN

"Mathematical Handbook for Scientists and Engineers",
Chapter 6 (2nd edition, McGraw-Hill, New York, 1968).

11. J.J. FIELD in "Plasma Physics and Nuclear Fusion Research",
ed. R.D. GILL (Academic Press, London, 1981).

12. W.A.J. PRIOR Culham Laboratory Report CLM-R241 (Edition 2) (March
1985).

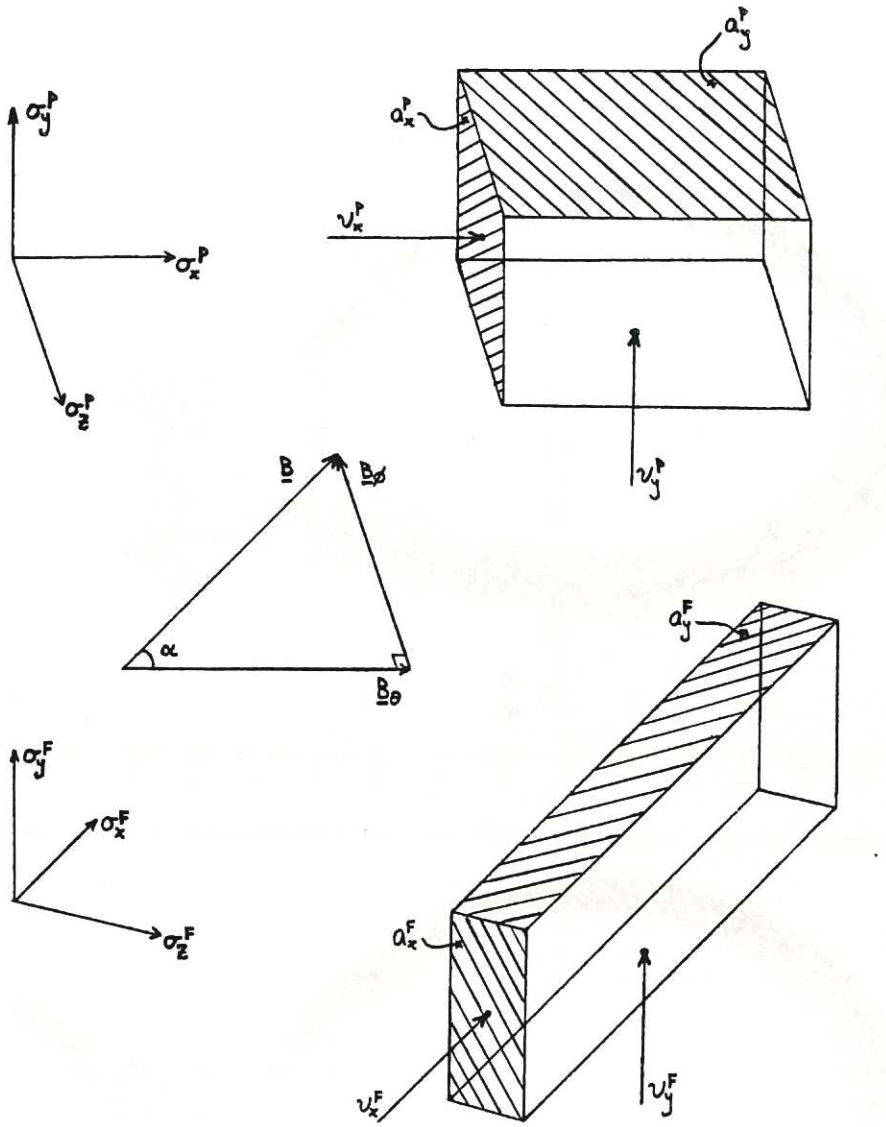


FIG. 1 Illustrative volume elements with pertinent facial areas and flow velocity components indicated in poloidal (top) and along field (bottom) co-ordinate frames.

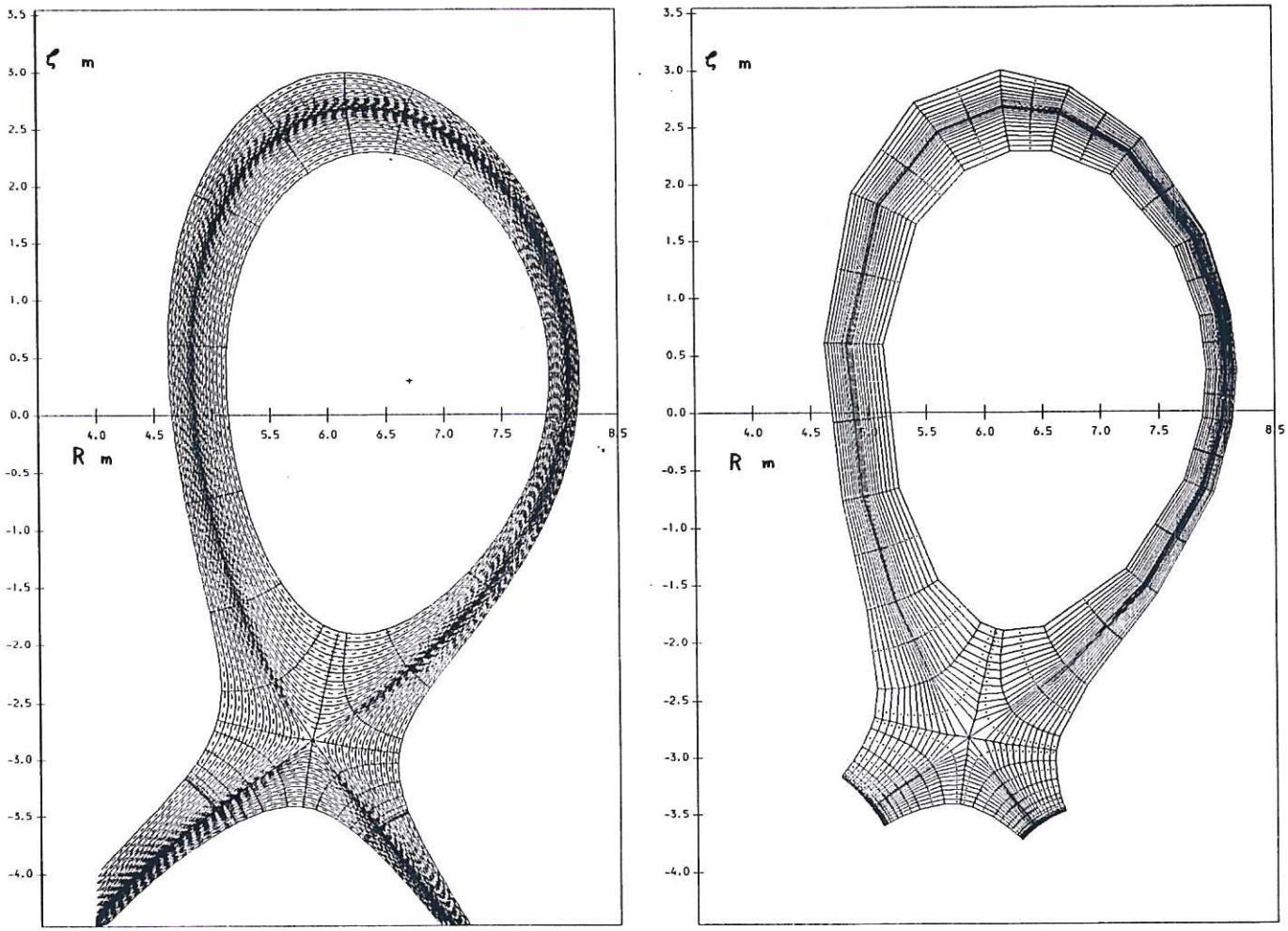


FIG. 2 Interpolated piecewise linear magnetic flux and orthogonal surfaces in poloidal plane for NET-3A single-null divertor (left). Corresponding discrete grid with cell centres shown (right).

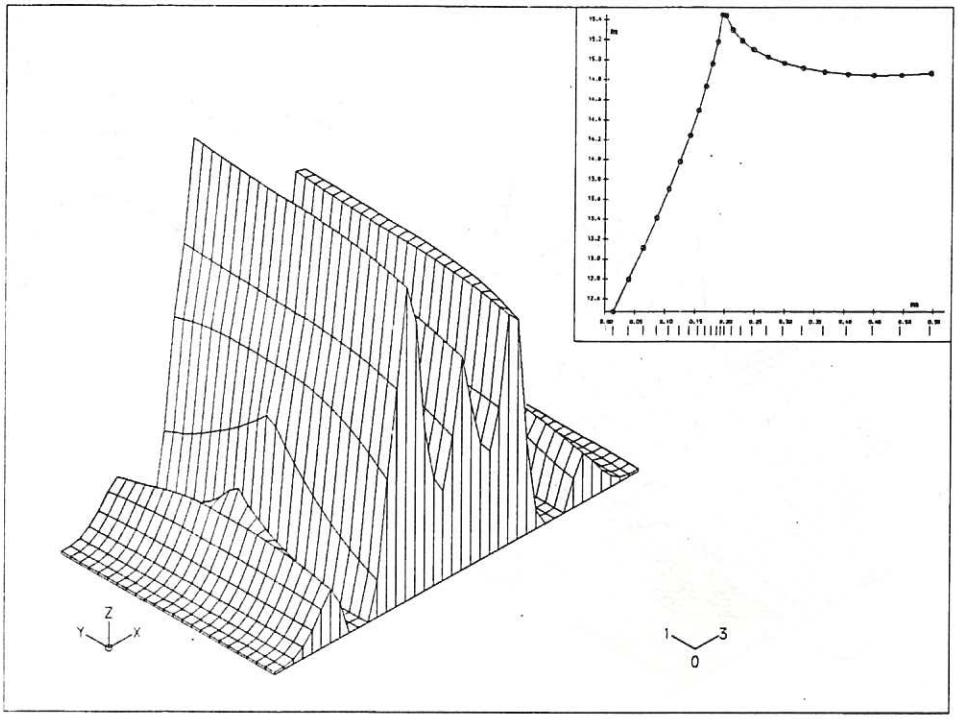


FIG. 3 Associated projection over grid indices of cell longitudinal diameters $ds_z^p$ in poloidal plane. Zero value channels reveal positions of grid cuts. Inset: total poloidal arc length along each grid row against initial mid-position on inner target, starting from innermost private flux surface. Recall lower half grid rows follow a divertor private contour up to first cut, then traverse its closed main torus counterpart to second cut, and finally complete the original private contour.

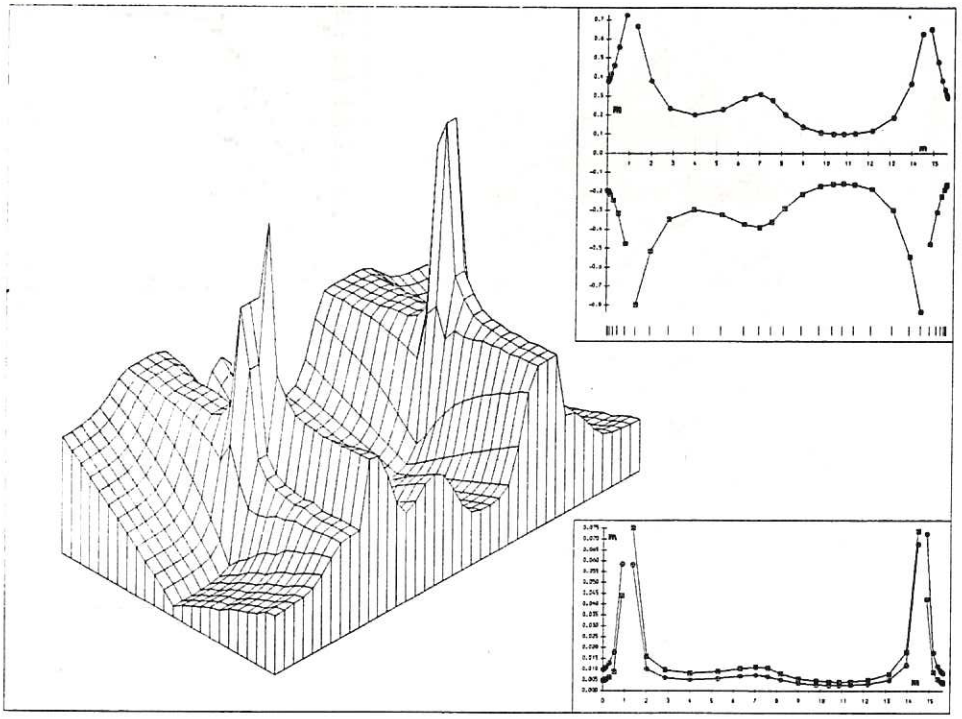

FIG. 4 Equivalent projection to FIG.3 for cell orthogonal diameters $ds_y$. Large value spikes again lie within grid cuts. Inset (upper): total poloidal width outside (positive) and inside (negative) separatrix across each grid column, against mid-position along separatrix, starting from inner target. Cut columns themselves are excluded. Inset (lower): cell orthogonal diameters $ds_y$ along grid rows immediately inside (x) and outside (+) separatrix against separatrix distance.

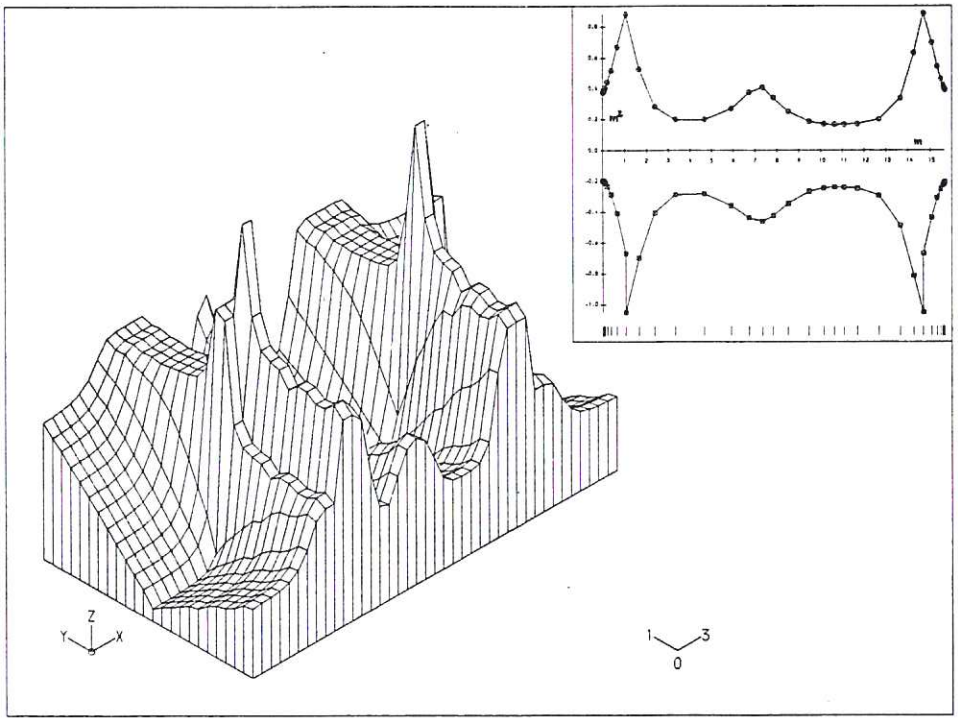


FIG. 5 Equivalent projection to FIG.3 for magnetic flux orthogonal interfacial areas $a_x^p$ in poloidal frame. Inset: sum interfacial areas outside (positive) and inside (negative) separatrix across each grid column, against distance along separatrix from inner target. Discontinuities across lower half grid cuts are evident.

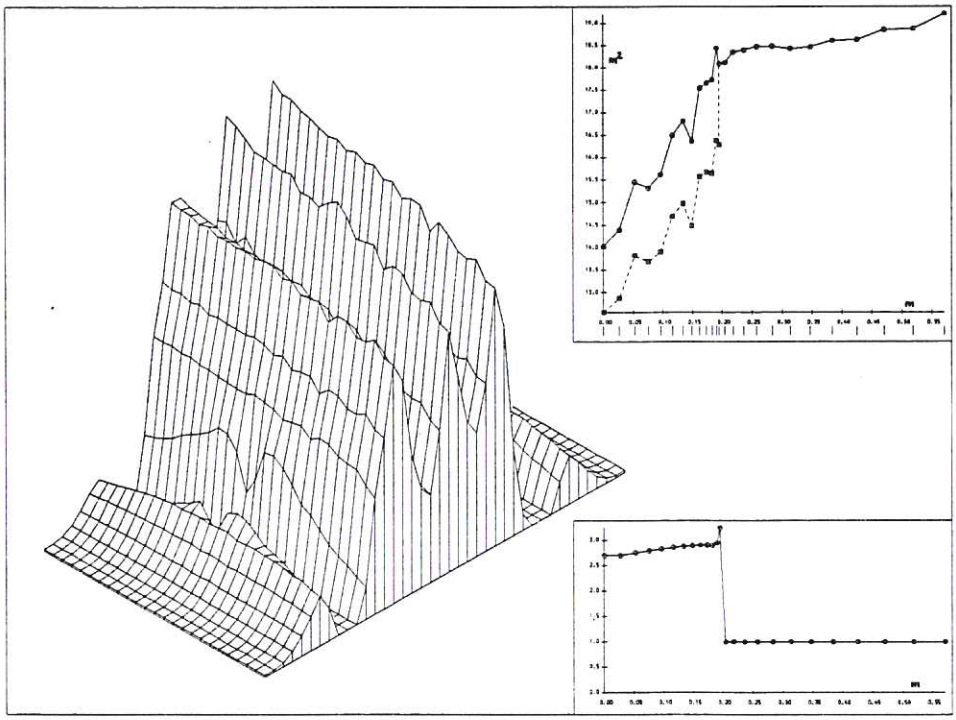

FIG. 6 Equivalent projection to FIG.3 for magnetic flux parallel interfacial areas $a_y$. Inset (upper): sum interfacial areas along each grid row (solid), and along closed main torus portions only (dashed), against initial position on inner target from innermost private flux contour. Inset (lower): Multiplicative factor applied over lower half grid cuts to symmetric toroidal normalisations of each row, against position across inner target. A smoother transition in total areas on either side of separatrix results.

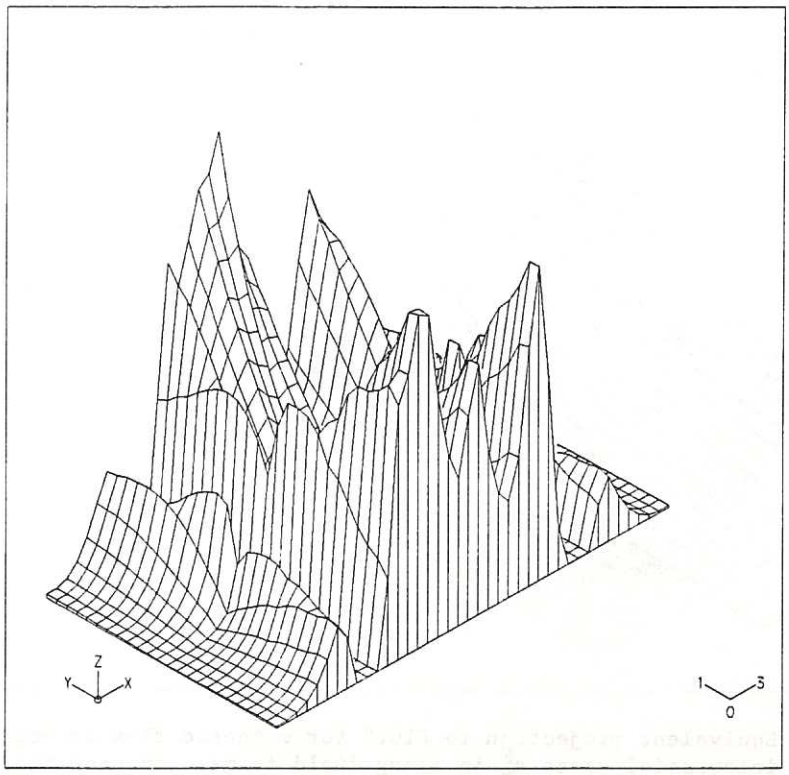


FIG. 7 Equivalent projection to FIG.3 for cell volumes V. Very small values adjacent to targets reflect clustering of grid both in facing high recycling regions and around separatrix.

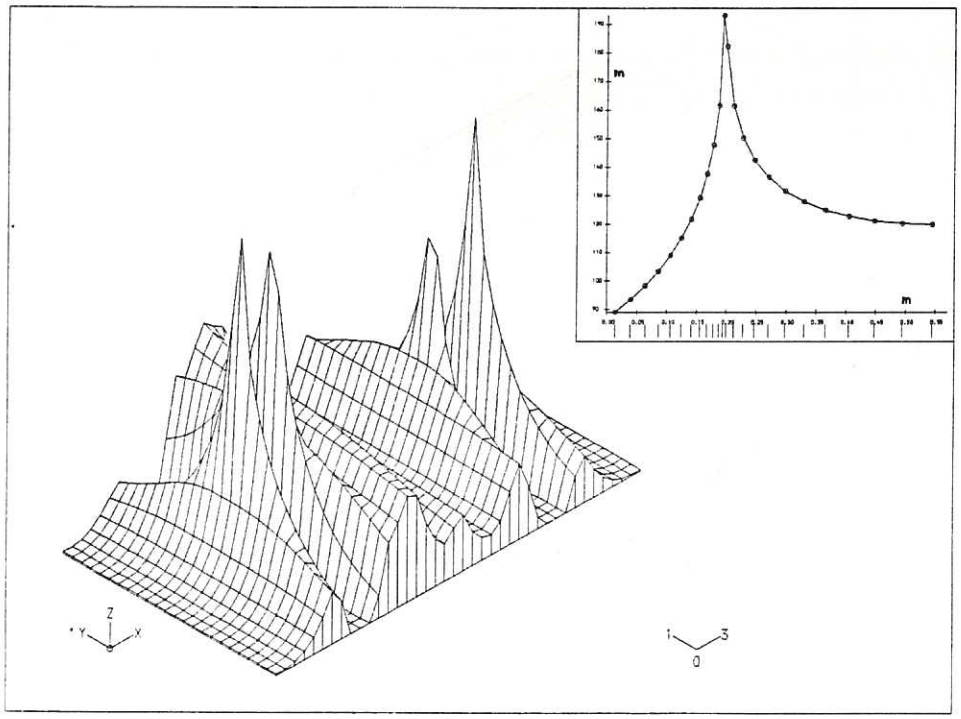


FIG. 8 Corresponding projection over grid indices of cell magnetic connection lengths $ds_x^F$ in along field frame. Shear is seen to be small except in immediate vicinity of poloidal field null (X-point). Inset: total connection lengths along each row against intercept across inner target.

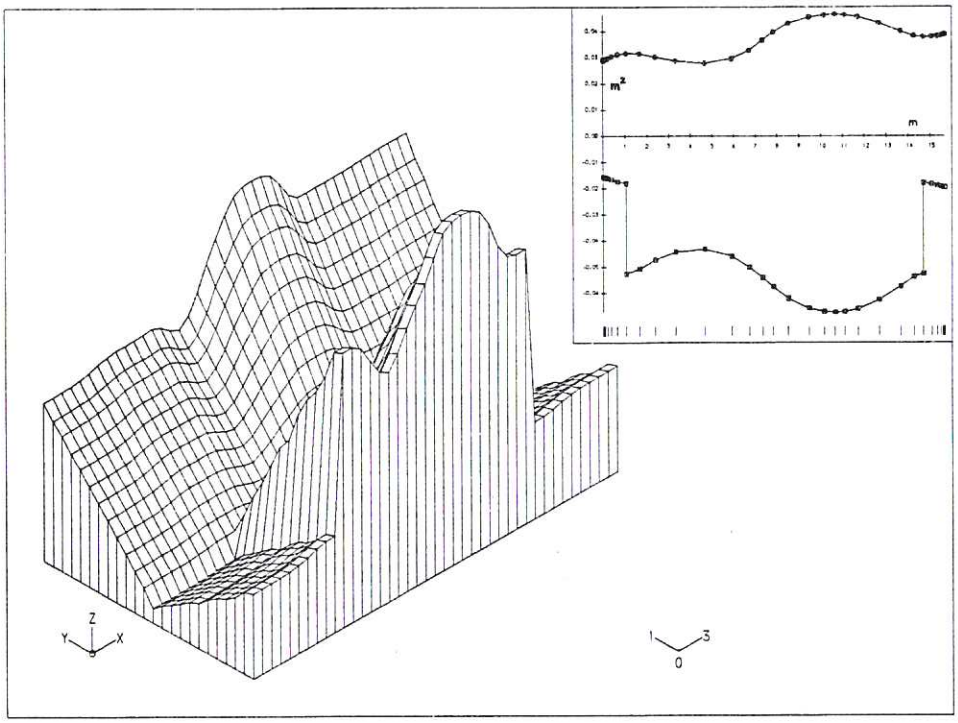

FIG. 9 Equivalent projection to FIG.8 for magnetic flux orthogonal interfacial areas $a_x^F$ in along field frame. An expected relation essentially to major radial co-ordinate is manifest. Inset: sum interfacial areas outside (positive) and inside (negative) separatrix across each grid column, against poloidal distance along separatrix from inner target.

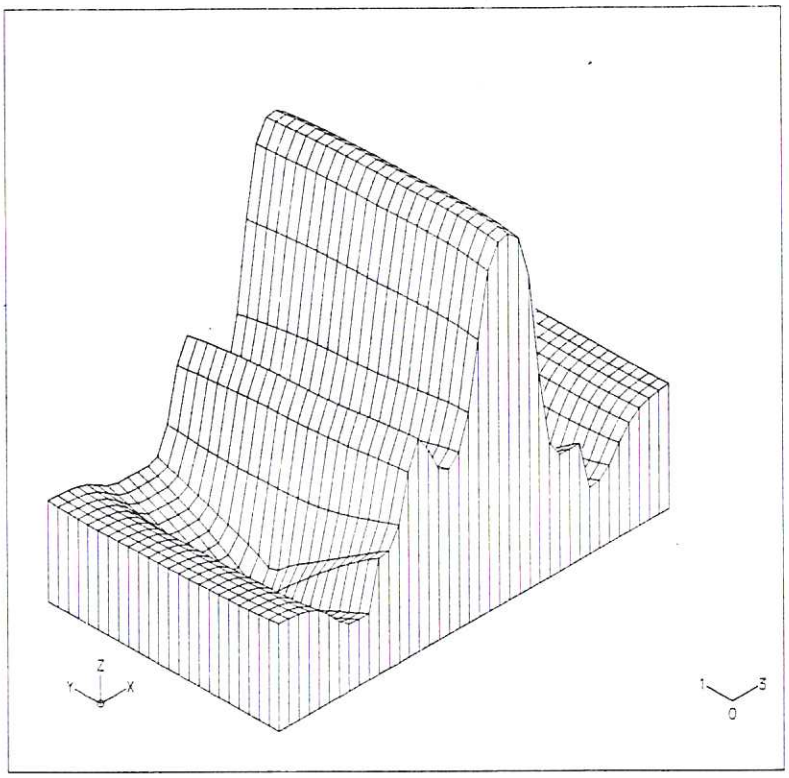

FIG. 10 Corresponding projection over grid indices of cosine of magnetic field line pitch angle ($B_\theta/B$). Values are connection length averages given by ratio of cell longitudinal diameters in poloidal and along field frames $ds_x^P(1/ds_x^F)$.

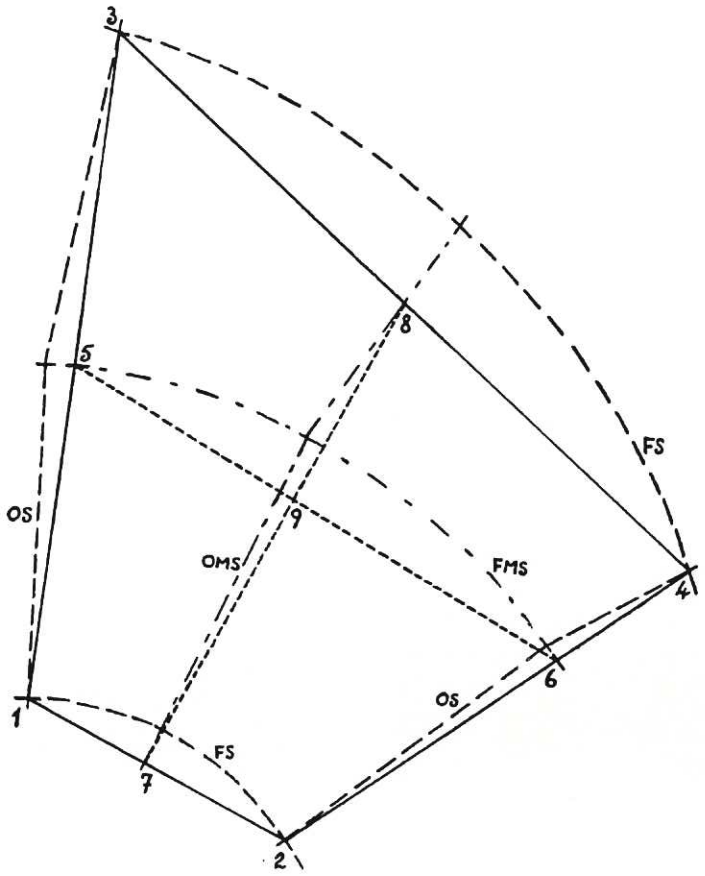


FIG. 11 Identification of ordered points defining basic discrete cell in poloidal plane between piecewise linear magnetic flux surfaces (FS), mid-surfaces (FMS) and orthogonal curves (OS) and mid-curves (OMS).